JOURNAL OF GUIDANCE, CONTROL, AND DYNAMICS
Vol. 31, No. 4, July–August 2008

Robust Linear Output Feedback Control of an Airbreathing Hypersonic Vehicle

David O. Sigthorsson,* Pete Jankovsky,* Andrea Serrani,† and Stephen Yurkovich‡
The Ohio State University, Columbus, Ohio 43210
and
Michael A. Bolender§ and David B. Doman¶
U.S. Air Force Research Laboratory, Wright–Patterson Air Force Base, Ohio 45433

DOI: 10.2514/1.32300

This paper addresses issues related to robust output-feedback control for a model of an airbreathing hypersonic vehicle. The control objective is to provide robust velocity and altitude tracking in the presence of model uncertainties and varying flight conditions, using only limited state information. A baseline control design based on a robust full-order observer is shown to provide, in nonlinear simulations, insufficient robustness with respect to variations of the vehicle dynamics due to fuel consumption. An alternative approach to robust output-feedback design, which does not employ state estimation, is presented and shown to provide an increased level of performance. The proposed methodology reposes upon robust servomechanism theory and makes use of a novel internal model design. Robust compensation of the unstable zero dynamics of the plant is achieved by using measurements of pitch rate. The selection of the plant's output map by sensor placement is an integral part of the control design procedures, accomplished by preserving certain system structures that are favorable for robust control design. The performance of each controller is comparatively evaluated by means of simulations of a full nonlinear model of the vehicle dynamics and is tested on a given range of operating conditions.

Nomenclature

D	=	drag
e	=	tracking error
e_m	=	model-following error
g	=	acceleration due to gravity
h	=	altitude
$h^\star$	=	altitude at trim
I_{yy}	=	moment of inertia
L	=	lift
M	=	pitching moment
m	=	mass
N_i	=	ith generalized elastic force
n_z	=	body axis normal acceleration at the center of gravity
$n_{z,f}$	=	measured body axis normal acceleration
Q	=	pitch rate
Q_f	=	pitch-rate measurement
r	=	reference command for y
T	=	Thrust
u	=	control input
u_a	=	auxiliary input for the stabilization of the zero dynamics
V_t	=	vehicle velocity
$V_t^\star$	=	vehicle velocity at trim
w	=	state of the reference model
x	=	state of the normal form of the plant
x_a	=	location of accelerometer
x_{cg}	=	location of center of gravity
x_{rg}	=	location of rate gyro
x_s	=	vector of sensor locations
x_{aug}	=	augmented state for linear-quadratic regulator design
x_f	=	variation of flexible states from trim
x_{rb}	=	variation of rigid-body states from trim
y	=	regulated output, $(V_t - V_t^\star, h - h^\star)^T$
y_a	=	auxiliary output for the stabilization of the zero dynamics
y_{aug}	=	augmented performance output for linear-quadratic regulator design
y_m	=	reference output for tracking error
y_{meas}	=	measured output
z	=	state of the zero dynamics of the plant
z^a, $\bar{z}^a$	=	state of the augmented zero dynamics
α	=	angle of attack
δ_c	=	canard deflection angle
$\delta_c^\star$	=	canard deflection angle at trim
δ_e	=	elevator deflection angle
$\delta_e^\star$	=	elevator deflection angle at trim
ζ	=	damping ratio of the reference generator
ζ_m	=	modal damping
η_i	=	ith mass-normalized mode shape
θ	=	pitch angle
μ	=	uncertain model parameter vector
μ_0	=	nominal value of the model parameter vector
ξ_0	=	state of the compensator for the zero dynamics
ξ_1	=	state of the dynamic extension
ξ_2	=	state of the internal model
ξ_3	=	state of the internal model
ϕ	=	fuel-to-air ratio
$\bar{\phi}_i$	=	ith mass-normalized mode shape
$\phi^\star$	=	fuel-to-air ratio at trim
$\omega_{m,i}$	=	ith modal frequencies
ω_n	=	natural frequency of the reference generator

Presented as Paper 6327 at the AIAA Guidance, Navigation, and Control Conference and Exhibit, Hilton Head, SC, 20–23 August 2007; received 22 May 2007; revision received 18 January 2008; accepted for publication 18 January 2008.

*Graduate Student, Department of Electrical and Computer Engineering, 2015 Neil Avenue.
†Assistant Professor, Department of Electrical and Computer Engineering, 2015 Neil Avenue. Member AIAA.
‡Professor, Department of Electrical and Computer Engineering, 2015 Neil Avenue.
§Aerospace Engineer, Air Vehicles Directorate, 2210 Eighth Street, Suite 21. Senior Member AIAA.
¶Senior Aerospace Engineer, Air Vehicles Directorate, 2210 Eighth Street, Suite 21. Associate Fellow AIAA.

I. Introduction

HYPERSONIC airbreathing vehicles offer a promising technology for cost-efficient access to space, because scramjet propulsion may provide significant advantages over traditional expendable rockets. The design of guidance and control systems for airbreathing hypersonic vehicles is a challenging task due to the unique characteristics of the vehicle dynamics. Strong couplings between propulsive and aerodynamic forces result from the underslung location of the scramjet engine. The length, slender geometry, and flexibility of the vehicle structure cause the vibrational modes to significantly affect the aerodynamic forces [1–5]. Most dynamic models of interest are shown to be unstable and of nonminimum phase with respect to the variables to be controlled [4]. In addition, significant uncertainties affect the model as a result of the variability of the vehicle characteristics with the flight conditions, fuel consumption, and thermal effects on the structure [6–8]. For linearized versions of these models, the most recent results available in the literature consider several configurations of increasing complexity. More specifically, adaptive controllers for a linearization of the computational fluid dynamics (CFD)-based model of Mirmirani et al. [9] are presented in [10–13], and the design of baseline linear controllers (which include antiwindup and constrained tracking control) is considered in [14–16] for the model proposed by Bolender and Doman [4]. A few recent contributions have also attempted design directly on nonlinear models [17–21].

Although the aforementioned works assume availability of measurements of the full state for feedback control, the more realistic case of output-feedback control is considered in this paper. Two different strategies are presented and discussed: a classic linear-quadratic observer-based controller (referred to as a *baseline design* and used mainly for comparison purposes) and an internal model controller based on an original formulation of robust servomechanism design [22–26]. A peculiar feature of this novel controller is that it does not rely on state estimation; hence, the closed-loop system is arguably less prone to inaccuracy due to model uncertainty than is the observer-based counterpart.

Among the results available in the literature, Davidson et al. [27] described the flight control system of NASA's Hyper-X vehicle [3], designed to provide aerodynamic surface commands for longitudinal and lateral-directional control. The longitudinal control law employs a gain-scheduling controller that uses estimated angle of attack and measured pitch rate as feedback signals. Various approaches to obtaining estimation of the angle of attack are described. The lateral-directional control loop has a similar structure and employs feedback from the bank angle, roll rate, and gravity-compensated yaw rate. Schmidt et al. [28–31] considered the design of linear multivariable strategies for output-feedback guidance and control of linearized models based on Chavez and Schmidt [1] and Bilimoria and Schmidt [2], using techniques from classic control theory. It is worth noting that the inner control loop proposed in [28,29] requires a measurement of engine pressure, measurements of pitch rates at two separate locations for active structural damping, and availability of angle of attack, either measured directly or synthesized (that is, observed) from acceleration measurements. Furthermore, the engine thrust is assumed to be available for feedback, although the issue of reconstructing this piece of information is not specifically addressed. The guidance loop [30,31] employs measurements of the vehicle's flight-path angle and longitudinal acceleration alongside those of altitude and velocity.

In the work presented in this paper, the control objective is to asymptotically track velocity and altitude reference commands for the longitudinal vehicle dynamics. Only the regulated outputs (velocity and altitude) are assumed to be available for feedback, together with measurements of pitch rate and normal acceleration (for the baseline controller) or pitch rate (for the internal model controller), which provide supplementary information on the state of the system. Because the location of these additional sensors along the longitudinal axis of the vehicle influences the coupling between rigid and flexible dynamics in closed loops, sensor placement is treated as an intrinsic part of the design process [32–35]. Compared with [28–31], the control strategies proposed in this paper integrate the guidance and control loops and offer the advantage of requiring a smaller number of sensors. On the other hand, the control inputs include an additional control surface: namely, a canard. The use of a canard was advocated by Bolender and Doman [36] as a means to addressing the strong nonminimum-phase characteristic of the flight-path-angle dynamics of the model [4].

Characteristic features of the flexible dynamics of airbreathing hypersonic vehicles are their variability with the flight conditions and the presence of unmodeled aerothermal effects [6,7]. As a result, any sensible control design for this class of aircraft must provide robustness against (possibly large) parametric uncertainty. This requirement indubitably poses a severe challenge for output-feedback design based on asymptotic state observation. Nonetheless, satisfactory results obtained using linear state-feedback control [14,15] naturally raise the question of whether a robust linear observer may suffice to supplement for incomplete knowledge of the states in the presence of model uncertainty. To provide an answer, a certainty-equivalence version of the linear-quadratic regulator with implicit model-following (LQR/IMF) described in [14] is first presented. The controller uses a full-order observer designed using a linear-quadratic estimator with loop transfer recovery (LQE/LTR) methodologies. A sensor placement strategy, similar to those proposed in [37–39], is employed with the intent of maximizing observability of the full state. In nonlinear simulation, the baseline control design is shown to provide insufficient robustness with respect to unmodeled nonlinearities and variations of the vehicle dynamics due to fuel consumption, adopted in this paper as a representative of generic model uncertainty. The loss of performance of the baseline controller, when applied to the nonlinear model, is attributed to the presence of the observer, despite the fact that the latter is verified to perform adequately on the linearized plant model. These considerations prompted the investigation of alternative techniques for output-feedback control that do not necessitate the use of asymptotic state observation.

The main contribution of this work is therefore to present an approach to robust output-feedback control design as an alternative to certainty-equivalence design, which is shown to yield better performance with respect to the observer-based baseline controller in nonlinear closed-loop simulations. The design reposes upon a novel formulation (based on singular-perturbation arguments) of the robust internal model design given by Isidori et al. [26], which is believed to be of its own methodological interest. The structural properties of the plant model (namely, the existence of vector relative degree with respect to the regulated output) are exploited to obtain a normal form that is amenable to robust stabilization. The canard deflection and the pitch-rate measurement are used as an auxiliary input/output pair to stabilize the zero dynamics of the system with respect to the controlled output. The placement of the rate gyro plays a role in obtaining robust stabilizability of the zero dynamics and serves as a controller parameter to be tuned appropriately. Then after precompensation of the zero dynamics, the system is controlled through the remaining inputs (fuel-to-air ratio and elevator surface deflection) and outputs (velocity and altitude). A dynamic extension and a robust servomechanism design based on timescale-separation methods is used to provide robust tracking control. Although the theoretical derivation of the internal model controller is ostensibly elaborate, the methodology is of general applicability and the selection of the gains proceeds along simple and intuitive lines.

The performances of the two controllers are evaluated and compared using simulations on the full nonlinear model of the vehicle dynamics for a large envelope of operating conditions. A thorough comparison between the two strategies in terms of their complexity and the tuning of the controller gains is also provided. It is shown that the robust internal model controller yields robust tracking over the whole range of parameter variations and for a larger set of operating conditions than with its observer-based counterpart. This capability of the internal model controller makes it suitable for implementation on a gain-scheduling flight control system, for which it is of importance to minimize the number of the interpolating compensators.

II. Model and Control Objectives

A. Airbreathing Hypersonic Vehicle Model

The hypersonic vehicle model considered in this paper is the assumed-modes version [8] of the model developed by Bolender and Doman [4]. In the cited references, the stability-axis equations of motion for the longitudinal dynamics of the hypersonic vehicle are derived using Lagrange's equations and compressible flow theory. Flexibility effects are included by modeling the vehicle as a single flexible structure, whereas the scramjet engine model is adopted from Chavez and Schmidt [1]. A sketch of the vehicle geometry showing the location of the control surfaces is given in Fig. 1. The nonlinear equations of motion used in this paper for analysis and simulation purposes are derived assuming a flat Earth and unit vehicle depth. The model comprises five rigid-body states and six flexible states, corresponding to the first three vibrational modes:

$$\begin{aligned}
&\dot{V}_t = \frac{1}{m}(T\cos\alpha - D) - g\sin(\theta-\alpha) \qquad \dot{h} = V_t\sin(\theta-\alpha)\\
&\dot{\alpha} = \frac{1}{mV_t}(-T\sin\alpha - L) + Q + \frac{g}{V_t}\cos(\theta-\alpha) \qquad \dot{\theta} = Q\\
&\dot{Q} = \frac{M}{I_{yy}} \qquad \ddot{\eta}_i = -2\zeta_m\omega_{m,i}\dot{\eta}_i - \omega_{m,i}^2\eta_i + N_i \qquad i = 1,2,3
\end{aligned} \tag{1}$$

The control inputs $(\phi, \delta_e, \delta_c)^T$ appear implicitly in Eq. (1) through the aerodynamic and generalized forces. The assumed-modes model developed in [8] considers the vehicle as a single flexible structure instead of clamped beams, as done originally in [4]. The vibrational system is defined as a traditional free-beam model [40] with mass-normalized mode shapes. The flexible modes are orthogonal to the rigid-body modes; therefore, the interaction between rigid and flexible dynamics occurs only through the aerodynamic forces. This results in a much more manageable nonlinear model for control design than with the original model, referred to as the "heave-coupling model" by Parker et al. [19]. Further details on the model and on the differences with [1,2,6] can be found in the cited references.

The structural dynamics are affected by parametric uncertainty due to unmodeled thermal effects [7] and by variability in the operating conditions. In particular, changes in node locations and modal frequencies of the flexible modes occur as the mass of the vehicle decreases with fuel consumption [8], whereas the damping ratio and the mode shapes themselves remain relatively constant. The

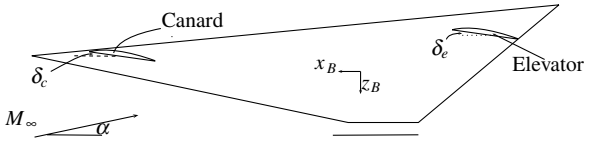

Fig. 1 Geometry of the hypersonic vehicle model.

Table 1 Vehicle mass, center of gravity, and modal frequencies at different fuel levels; bold entries denote the nominal operating condition

Fuel Level	0%	30%	50%	70%	100%
m, slug/ft	93.57	126.1	**147.9**	169.6	202.2
x_{cg}, feet from nose	53.1	53.61	**53.82**	53.98	54.16
$\omega_{m,1}$, rad/s	22.78	21.71	**21.17**	20.73	20.17
$\omega_{m,2}$, rad/s	68.94	57.77	**53.92**	51.24	48.4
$\omega_{m,3}$, rad/s	140	117.8	**109.1**	102.7	95.6

four sets of curves in Fig. 2 show the behavior of the mode shapes as fuel is consumed. An example of variation in modal frequency and in node, antinode, and center-of-gravity locations for various fuel conditions is listed in Table 1. For all conditions, the damping ratio of all modes is constant: $\zeta_m = 0.02$. In the table, the parameters corresponding to the 50% fuel level, highlighted in bold, define the nominal operating condition. Because a dynamic fuel-consumption model has not yet been incorporated, the vehicle mass will be held constant in simulations. However, the coefficients of the flexible model will be considered as uncertain parameters ranging within the intervals given in Table 1, corresponding to 100% variation in fuel level. On one hand, this approach is motivated by the fact that the vehicle mass changes on a much slower timescale than with the flexible dynamics. On the other hand, the considered setup will serve, for the purpose of robust control design, as a representative of more general scenarios in which the flexible dynamics are affected by parametric uncertainty, possibly including aerothermal effects [41].

For control design, the equations of motion (1) are linearized about a trim condition, yielding the linear parameter-dependent model:

$$\begin{aligned}
\dot{x}_{\text{rb}} &= A_{11}(\mu)x_{\text{rb}} + A_{12}(\mu)x_f + B_1(\mu)u\\
\dot{x}_f &= A_{21}(\mu)x_{\text{rb}} + A_{22}(\mu)x_f + B_2(\mu)u \qquad y = Cx_{\text{rb}}
\end{aligned} \tag{2}$$

where $x_{\text{rb}} \in \mathbb{R}^5$, $x_f \in \mathbb{R}^6$, and $u \in \mathbb{R}^3$ denote, respectively, the variation of the rigid-body states, the flexible states, and the control inputs from their respective trim values. The regulated output $y = (V_t - V_t^\star, h - h^\star)^T$ comprises the deviation of the vehicle velocity and the vehicle attitude from trim. The vector $\mu \in \mathbb{R}^p$ denotes uncertain parameters (mass, location of the center of gravity, natural frequencies of the flexible modes, etc.) due to variations in the operating conditions and fuel level. The range of variation of the entries of μ, represented as a fixed compact set $\mathcal{P} \subset \mathbb{R}^p$, is obtained from the entries in Table 1. The nominal value of the parameter vector, denoted by μ_0, is computed at the equilibrium point at trim given in Table 2, in which the nominal operating condition of 50% fuel level is assumed.

B. Sensor Models

Although our previous work on control design for the linearized model (2) assumed availability of measurements of the full states x_{rb} and x_f for feedback [14–16], in this paper, the more realistic case of

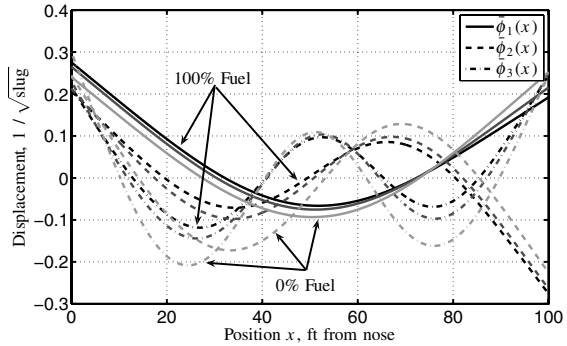

a) Mass-normalized flexible mode shapes

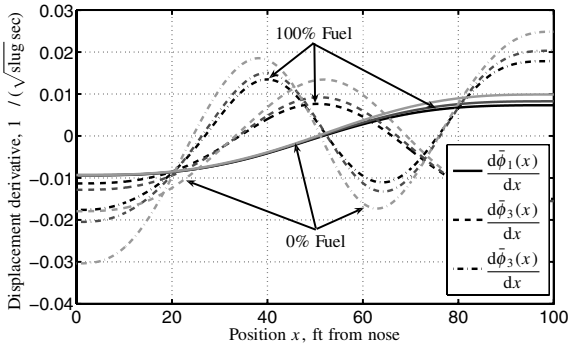

b) Mass-normalized mode shape derivatives

Fig. 2 Mass-normalized flexible mode shapes and their derivatives for various fuel levels: empty, 50% full, and 100% full.

Table 2 Nominal trim condition at 50% fuel level

Rigid-body states		Flexible states		Inputs	
V_t	7846.4 ft/s	η_1	0.594 ft$\sqrt{\text{slug}}$	ϕ	0.120
h	85,000 ft	η_2	−0.0976 ft$\sqrt{\text{slug}}$	δ_e	0.120 rad
α	0.0219 rad	η_3	−0.0335 ft$\sqrt{\text{slug}}$	δ_c	−0.0914 rad
θ	0.0219 rad	$\dot{\eta}_i$	0 ft$\sqrt{\text{slug}}$/s, $i = 1, 2, 3$		
Q	0 rad/s^2				

output-feedback design is considered. For obvious reasons, it is assumed that measurements of the regulated output y are available to the controller. In addition, supplementary information is provided by a rate gyro and an accelerometer. The pitch rate measured by a rate gyro located at x_{rg} is given by [37]

$$Q_f = Q - \sum_{i=1}^{n} \frac{\mathrm{d}\bar{\phi}_i(x_{\text{rg}})}{\mathrm{dx}} \dot{\eta}_i \tag{3}$$

where n is the number of flexible modes. An indirect estimation of the angle of attack of the aircraft can be obtained from measurements of normal acceleration [42]. Because the vehicle model only considers longitudinal motion, the rolling motion is neglected, and the normal acceleration at the center of mass (normalized to g units) is given in the body axes by

$$\frac{n_z}{g} = \frac{-D\sin\alpha}{mg} - \frac{L\cos\alpha}{mg} + \cos\theta \tag{4}$$

When the accelerometer is positioned away from the center of gravity, the measurement of the body normal acceleration is given by a combination of n_z and contributions from the rigid-body pitch acceleration and the acceleration due to the vehicle elasticity: namely,

$$n_{z,f} = n_z - \frac{1}{g}(x_{\text{cg}} - x_a)\dot{Q} + \frac{1}{g}\sum_{i=1}^{n} \bar{\phi}_i(x_a)\ddot{\eta}_i \tag{5}$$

where x_a is the location of the accelerometer along the longitudinal body axis. Although the pitch-rate measurement equation (8) is linear, the relationships (4) and (5) must be linearized about the trim condition to be incorporated into the model. The general expression of the measured output for the linearized model (including velocity and altitude) is given as

$$y_{\text{meas}} = C_{\text{rb}}(\mu, x_s)x_{\text{rb}} + C_f(\mu, x_s)x_f + D(\mu, x_s)u \tag{6}$$

where it is emphasized that output depends on the vector of sensor locations $x_s = (x_{\text{rg}}, x_a)^T$ and on the uncertain parameter vector μ. It must be kept in mind that the presence of the feedthrough term $D(\mu, x_s)$ is due to the accelerometer only.

C. Reference Model

The control objective is to perform robust tracking of reference trajectories for the regulated output y under the considered model parameter uncertainty. To facilitate comparison with our earlier work [14,15], the commands are generated as step signals filtered by a second-order reference model. The reference generator is modeled by the autonomous system:

$$\dot{w} = Sw \qquad r = Qw \tag{7}$$

where

$$w = (w_1, w_2)^T \in \mathbb{R}^6, \qquad r = (r_1, r_2)^T \in \mathbb{R}^2$$

$$S = \text{diag}(S_1, S_2) \qquad Q = \text{diag}(Q_1, Q_2)$$

$$S_i = \begin{pmatrix} 0 & 1 & 0 \\ -\omega_n^2 & -2\zeta\omega_n & \omega_n^2 \\ 0 & 0 & 0 \end{pmatrix} \qquad Q_i = (1 \quad 0 \quad 0) \qquad i = 1, 2$$

The assumption that both filters have the same damping ratio ζ and natural frequency ω_n is made here only for notational convenience and can be relaxed in an obvious manner. In Eq. (7), the outputs r_1 and r_2 denote, respectively, velocity and altitude reference.

For increased fidelity, the nonlinear model (1) includes appropriate saturations and rate limiters at the plant input, set at ± 0.52 rad and ± 1.047 rad/s, respectively, for the control surfaces δ_e and δ_c. The fuel-to-air ratio is constrained in the range $\phi \in [0, 1]$ and includes a linear first-order lag with time constant $\tau = 0.1$ s. Although antiwindup schemes have been shown to provide a viable strategy to more directly accommodate the presence of input constraints [16], in this study, the constraints are accounted for indirectly by a proper tuning of the controller gains, including the parameters of the shaping filter in the reference model. Because the airbreathing hypersonic vehicle is not intended for highly aggressive maneuvers, the damping ratio and the natural frequency of the filter can be tuned to ensure that the control signals remain within the rate and saturation limits. In all subsequent simulation studies, the parameters of the prefilter were fixed at $\zeta = 0.9$ and $\omega_n = 0.039$, respectively; this results in a 2% settling time of about 121 s, with 0.2% overshoot. A typical reference to be tracked used in the simulation consists of a step-altitude increment of 10,000 ft and a velocity increment of 1000 ft/s from trim.

III. Baseline Controller Design

The baseline controller employed in this study for comparison with the proposed robust design is derived on the basis of the separation principle by using a state-feedback design in combination with a full-order observer. For the problem at hand, the state-feedback controller is provided by the results of Groves et al. [14], whereas a full-order observer is designed for the nominal model (2) once a suitable sensor configuration is selected.

As discussed by Bolender and Doman [4] and Williams et al. [8], the linearized model in Eq. (2) possesses an unstable short-period mode and a very lightly damped phugoid mode. The phugoid mode at $\omega = 0.036$ rad/s is clearly noticeable in the Bode plot of the singular values of the transfer-function matrix of the plant from the control input u to the regulated output y, shown in Fig. 3a. It must be noted that due to the fact that the dimension of the regulated output ($\dim y = 2$) is strictly smaller than the dimension of the control input ($\dim u = 3$), the transfer-function matrix has no transmission zeros, and hence, in principle, there are no a priori performance limitations if a state-feedback control is adopted. The state-feedback controller is thus designed to ensure stability in closed loops and to provide adequate tracking performance when assigning a closed-loop bandwidth well below the natural frequency of the first flexible mode. The methodology followed for the selection of the feedback gain is based upon the LQR design with implicit model-following [42]. Here, we limit ourselves to give a brief account of the method and refer the reader to the cited references for details.

After augmentation with the integral error

$$x_I = \int_0^t [y(\tau) - r(\tau)]\,\mathrm{d}\tau$$

the plant dynamics are written in the form

$$\dot{x}_{\text{aug}} = A_{\text{aug}}(\mu)x_{\text{aug}} + B_{\text{aug}}(\mu)u + G_{\text{aug}}r \qquad y_{\text{aug}} = C_{\text{aug}}x_{\text{aug}} \tag{8}$$

where $x_{\text{aug}} = (x_{\text{rb}}^T, x_f^T, x_I^T)^T$, $y_{\text{aug}} = (y^T, x_I^T)^T$, and the systems matrices are defined accordingly. Next, a reference model for the augmented tracking error, $e_{\text{aug}} = (y^T - r^T, x_I^T)^T$, is defined as the autonomous system:

$$\dot{y}_m = A_m y_m$$

with state $y_m \in \mathbb{R}^4$, where the Hurwitz matrix A_m specifies the desired asymptotically stable dynamics for the tracking error. Typically, A_m is selected as a diagonal matrix to enforce decoupling of the regulated output variables. The model-following error

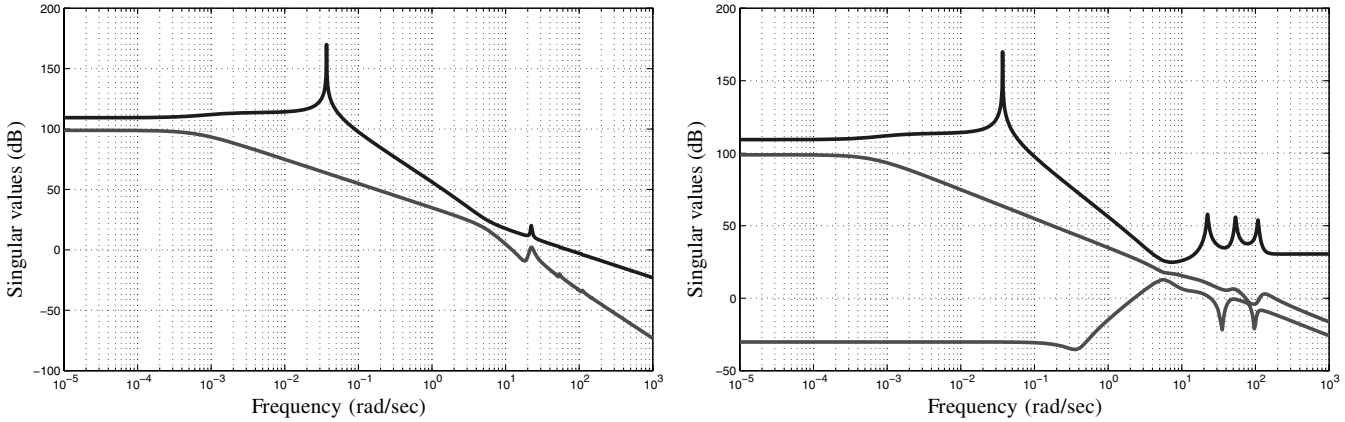

a) Plant transfer function matrix from u to y **b) Plant transfer function matrix from u to y_{meas}**

Fig. 3 Singular value plots of the plant transfer-function matrices; nominal operating conditions.

$$e_m = \dot{e}_{\text{aug}} - A_m e_{\text{aug}} \tag{9}$$

is used as a performance output for an infinite-horizon LQ optimization with cost function:

$$J_m = \int_0^\infty (e_m^T(\tau) Q_m e_m(\tau) + u^T(\tau) R_m u(\tau))\, \mathrm{d}\tau$$

where $Q_m \in \mathbb{R}^{4\times 4}$ and $R_m \in \mathbb{R}^{3\times 3}$ are positive-definite weighting matrices to be selected. Substituting the expression of e_m from Eq. (9) and using the nominal value of the model parameter vector in Eq. (8) will yield a standard LQ cost function in terms of the original state variables, for which the solution of the associated LQR optimization problem can be obtained via the solution of standard algebraic Riccati equations [42]. In synthesis, the IMF approach gives a convenient methodology for selecting the weighting matrices of the cost function in an LQR design. The solution of the LQ optimization yields the state-feedback controller:

$$u = -K_{\text{rb}} x_{\text{rb}} - K_f x_f - K_I x_I - K_w w$$

For asymptotic state reconstruction, both a rate gyro and an accelerometer are employed in addition to the velocity and altitude sensors, as discussed in Sec. II.B. Consequently, the measured output (6) for the baseline design is given by

$$y_{\text{meas}} = (V_t - V_t^\star, h - h^\star, Q_f, n_{z,f})^T$$

Because the focus is on asymptotic reconstruction of the full state of system (2) (including the states of the flexible dynamics), the selection of the sensor location is performed with the intent of maximizing observability of the system throughout the intended envelope of operating conditions. Thus, a well-placed sensor suite for the baseline controller must produce measurements containing information not only about the rigid-body states, but also about the vibrational components. The Popov–Belevitch–Hautus (PBH) observability test [43] was applied to determine the observability index of the linearized system (2) for the considered range of values for μ. The PBH test was preferred over the classic observability test, because the latter proved to be numerically ill-conditioned for the given plant model, even after appropriate scaling and balancing. Provided that the test matrices

$$\text{PBH}\,(\lambda_i, A, C) = (\lambda_i I - A^T C^T)$$

have full rank for each eigenvalue λ_i of A, their condition numbers provide an estimate of how close (A, C) is to being unobservable (the higher the condition numbers, the closer the pair is to being unobservable.) The condition number was then used as a performance index in an optimization process to search for the best location of the sensors; namely, the cost function is defined as

$$J(x_s) = \max_{i\in\{1,\ldots,n\}} \max_{\mu\in\mathcal{P}} \text{cond}(\text{PBH}(\lambda_i, A(\mu), C(\mu, x_s))) \tag{10}$$

and the objective is to minimize $J(x_s)$ with respect to the . Figure 4a shows an example of a typical variation of $J(x_s)$ with the positioning of one rate gyroscope when μ is fixed at its nominal value μ_0. Equation (3) clearly shows that placing a rate-gyroscope sensor at an antinode of the dominant mode shape will minimize the contribution of the flexible states to Q_f, whereas the measured output will contain richer information about the flexible state if the rate gyroscope is placed at locations corresponding to high values of $\mathrm{d}\bar{\phi}/\mathrm{dx}$. This is confirmed by comparison of Figs. 4a and 4b. Similarly, for a single accelerometer, the analysis of the performance index reveals that peaks of the cost function correlate with locations at which components of $\bar{\phi}(x_s)$ vanish. Following the optimization procedure, the final selection of the sensor suite employed for the baseline control design is a rate gyroscope placed at 1 ft and an accelerometer placed at 99 ft from the nose of the aircraft. Figure 3b shows the Bode plot of the singular values of the transfer-function matrix of the plant from the control input to the measured output for the given selection of the sensors' location. In the figure, the presence of the three flexible modes affecting the pitch rate and the acceleration measurements is clearly visible. Note that the maximum singular value of the transfer-function matrix does not roll off, due to the feedthrough term introduced by the accelerometer.

The expression of the observer-based feedback controller is given by

$$\begin{aligned}
\begin{pmatrix} \dot{\hat{x}}_{\text{rb}} \\ \dot{\hat{x}}_f \end{pmatrix} &= \begin{pmatrix} A_{11}(\mu_0) & A_{12}(\mu_0) \\ A_{21}(\mu_0) & A_{22}(\mu_0) \end{pmatrix} \begin{pmatrix} \hat{x}_{\text{rb}} \\ \hat{x}_f \end{pmatrix} + \begin{pmatrix} B_1(\mu_0) \\ B_2(\mu_0) \end{pmatrix} u \\
&\quad + L_{\text{obs}}(y_{\text{meas}} - \hat{y}_{\text{meas}}) \\
\hat{y}_{\text{meas}} &= C_{\text{rb}}(\mu_0, x_s)\hat{x}_{\text{rb}} + C_f(\mu_0, x_s)\hat{x}_f + D(\mu_0, x_s)u \\
u &= -K_{\text{rb}}\hat{x}_{\text{rb}} - K_f\hat{x}_f - K_I x_I - K_w w
\end{aligned} \tag{11}$$

where the feedback gains K_{rb}, K_f, K_I, and K_w are those obtained from the solution of the state-feedback IMF problem. It should be mentioned that in the actual implementation of the controller (11), the velocity and altitude estimates are discarded and replaced by their available measurements. The observer gain L_{obs} is computed by solving a dual LQE problem in which the selection of the weights of the cost functions is performed using the LTR technique [44–46]. Specifically, the LQE/LTR problem is set as the design of a Kalman filter with covariance matrices $Q_n > 0$ and $R_n > 0$ for the state noise and the measurement noise, respectively. The covariance matrix Q_n is selected as

$$Q_n = M_0 + qB(\mu_0)B^T(\mu_0)$$

where $M_0 > 0$ is a nominal covariance and $q > 0$ is a scalar tuning parameter. As $q \to \infty$, the solution of the associated LQE problem

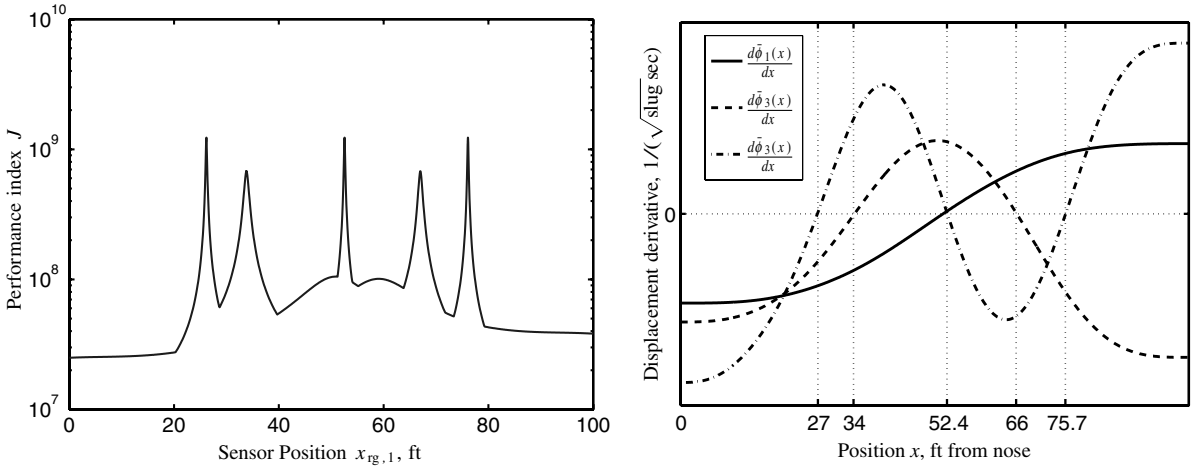

a) Observability vs rate-gyro position **b) Mode shapes derivatives**

Fig. 4 Effect of placement of a rate gyro on observability; nominal operating conditions.

yields an observer that asymptotically recovers the loop transfer function obtained when using full state feedback. The final selection of the weighting functions is as follows:

For LQR/IMF parameters,

$$A_m = 10^{-2} \times \text{diag}(-2, -1, -1, -0.5)$$
$$Q_m = 10^{-1} \times \text{diag}(0.1, 0.01, 1, 0.1)$$
$$R_m = 10^{3}\text{diag}(1, 180/\pi, 180/\pi)$$

For LQE/LTR parameters,

$$x_{\text{rg}} = 1 \text{ ft}$$
$$M_0 = 10^{-7} \times \begin{pmatrix} C_{\text{rb}}^T(\mu_0, x_s)C_{\text{rb}}(\mu_0, x_s) & C_{\text{rb}}^T(\mu_0, x_s)C_f(\mu_0, x_s) \\ C_f^T(\mu_0, x_s)C_{\text{rb}}(\mu_0, x_s) & C_f^T(\mu_0, x_s)C_f(\mu_0, x_s) \end{pmatrix}$$

$$x_a = 99 \text{ ft} \qquad R_n = 10^{-2} \times \text{diag}(10^{-2}, 1, 10^{-4}, 10^{4})$$

The Bode plot of the singular values of the closed-loop transfer-function matrix from r to y (reported in Sec. IV.B) show that the closed-loop bandwidth is placed well below the frequency of the first bending mode.

It is important to keep in mind that although the transfer function of the state observation loop (that is, the transfer-function matrix from u to y_{meas}) has no transmission zeros,** in the case considered here, the presence of the direct feedthrough term $D(\mu, x_s)$ limits the recovery of the loop gain that can be obtained via the LTR method. As a result, the loop gain achievable under state feedback cannot be fully recovered. This limitation cannot be circumvented by removing the accelerometer from the sensor suite, because in that case, the resulting (square) transfer-function matrix would possess a transmission zero at the origin due to the altitude dynamics, which again limits the applicability of LTR. Nonetheless, the LQE/LTR methodology yielded an observer design that was shown to provide, in conjunction with the IMF controller, stable tracking for the *linearized model* (2) in all fuel conditions while maintaining the control effort within the given bounds.

The good tracking performance of the baseline design achieved on the linearized model, however, did not carry over to simulations on the nonlinear model. Although satisfactory results were obtained in nominal operating conditions, as can be observed from Fig. 5, the baseline controller failed to maintain closed-loop stability when the fuel level was changed from the nominal value. Figure 6 shows the loss of tracking performance and instability occurring on the angle of attack, the pitch angle and their estimates, and the estimates of the flexible state when the fuel level is increased to 60%. Note that the original *state-feedback* IMF controller was verified to perform adequately in closed-loop nonlinear simulations at all fuel levels. This consideration seems to support the intuition that the loss of stability of the closed-loop system may be attributed to insufficiently robust state reconstruction (see, in particular, Figs. 6c and 6d).

**This is due to the fact that, this time, the dimension of the measured output ($\dim y_{\text{meas}} = 4$) is *strictly greater* than the dimension of the input.

IV. Robust Servomechanism Design

A numerical investigation of the parameterized model (2) revealed that the system matrices of the flexible dynamics are, as expected, much more sensitive to variations of μ than are the matrices associated with the rigid-body dynamics. Furthermore, the dependence of $n_{z,f}$ on the control input by way of the feedthrough map $D(\mu, x_s)$ was found to have a negative impact on the robustness of the closed-loop system. As μ deviates from its nominal value, cancellation of the term $D(\mu, x_s)u$ in the observation-error equation is not possible, and this creates a nonminimum-phase effect for the open-loop system augmented with the dynamic compensator (11). Ultimately, a decision was made to remove the accelerometer from the sensor suite and retain the rate gyro, resulting in a configuration employing the same number of control inputs and measured outputs. Note, however, that the dimension of the vector of controlled outputs y remains smaller than the dimension of the control input vector. This redundancy is indeed exploited in the controller presented in this section.

To set the stage for a new controller design, the normal form of system (2) with respect to the regulated output is computed using the procedure described in Sec. 5.1 of [47]. It turns out that for any $\mu \in \mathcal{P}$, system (2) has a well-defined vector relative degree of 1 or 2 with respect to the regulated output y and thus possesses an eight-dimensional zero dynamics. Next, we split the available inputs and outputs into two pairs:

$$(u_a, y_a) = (\delta_c - \delta_c^\star, Q_f)$$
$$(u_b, y) = ((\phi - \phi^\star, \delta_e - \delta_e^\star)^T, (V_t - V_t^\star, h - h^\star)^T)$$

where (u_a, y_a) will be used to control the zero dynamics, and (u_b, y) will be used for output tracking. In correspondence to this selection, the normal form of system (2) is written as

$$\begin{aligned} \dot{z} &= F(\mu)z + G(\mu)u_a + J_{11}(\mu)x \\ \dot{x} &= A(\mu)x + B(\mu)u_b + J_{21}(\mu)z + J_{22}(\mu)u_a \qquad y = Cx \\ y_a &= H(\mu, x_{\text{rg}})z + J_{12}(\mu)x \end{aligned} \tag{12}$$

where the state $x \in \mathbb{R}^3$ is defined as $x = (V_t - V_t^\star, h - h^\star, \dot{h})^T$, the state $z \in \mathbb{R}^8$ is obtained through a nonsingular transformation

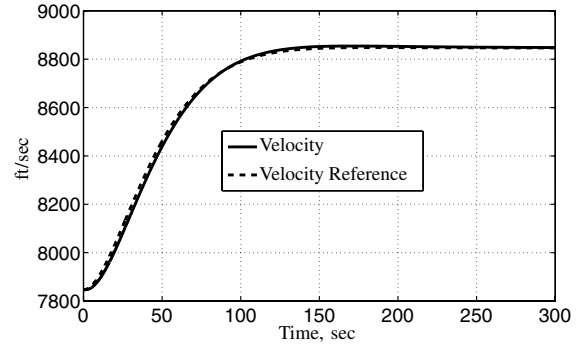

a) Velocity tracking

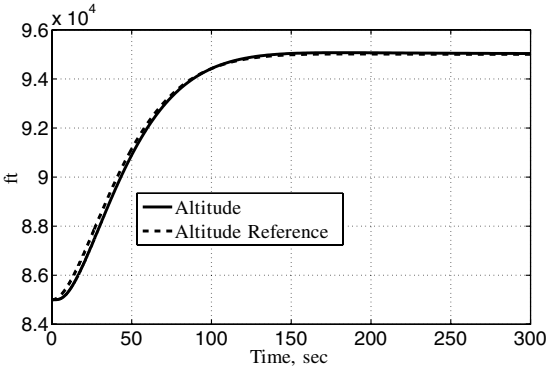

b) Altitude tracking

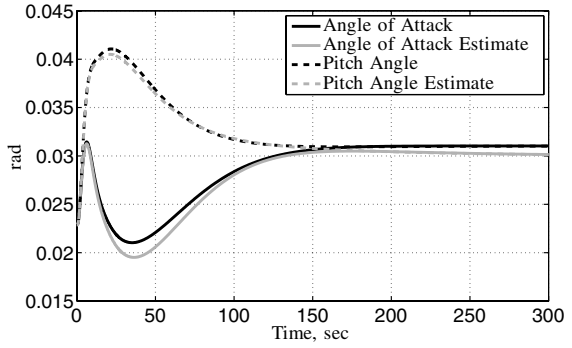

c) Angle of attack, pitch angle, estimates

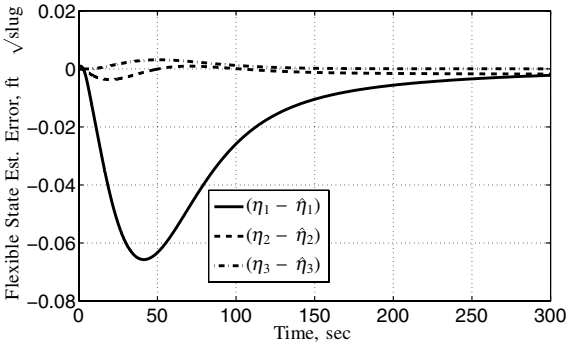

d) Observation error for the flexible states

Fig. 5 Output tracking and observer performance for the baseline controller; nonlinear simulations; fuel level 50%.

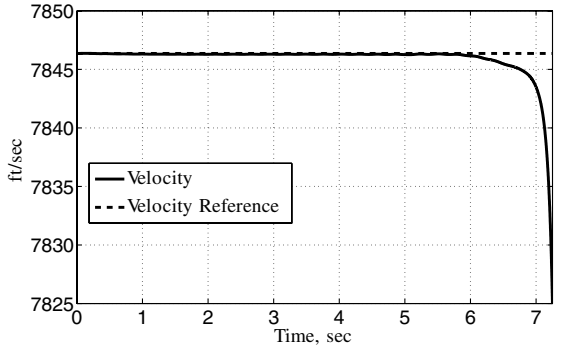

a) Velocity tracking

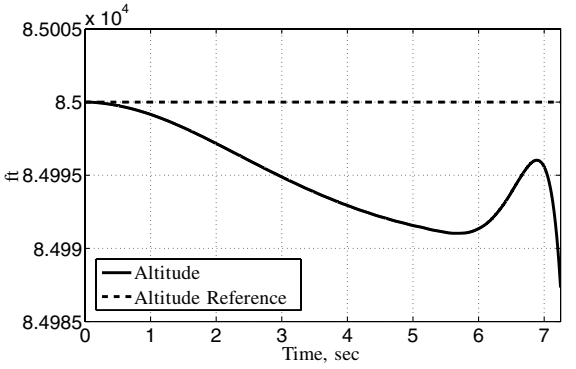

b) Altitude tracking

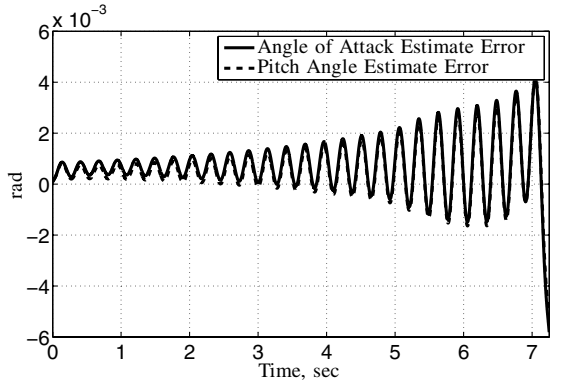

c) Angle of attack, pitch angle estimation error

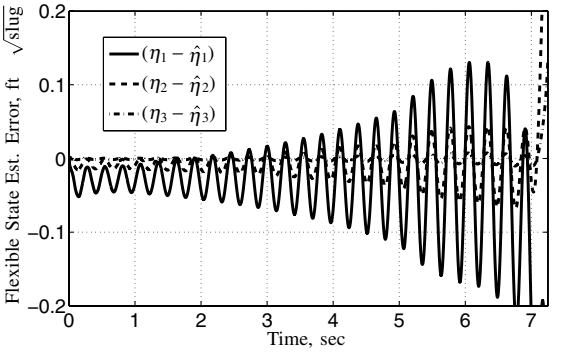

d) Observation error for the flexible states

Fig. 6 Output tracking and observer performance for the baseline controller; nonlinear simulations; fuel level 60%.

involving both the flexible and the rigid-body states, and the triplet $(A(\mu), B(\mu), C)$ has the form

$$A(\mu) = \begin{pmatrix} a_{11}(\mu) & a_{12}(\mu) & a_{13}(\mu) \\ 0 & 0 & 1 \\ a_{31}(\mu) & a_{32}(\mu) & a_{33}(\mu) \end{pmatrix}$$

$$B(\mu) = \begin{pmatrix} b_{11}(\mu) & b_{12}(\mu) \\ 0 & 0 \\ b_{31}(\mu) & b_{32}(\mu) \end{pmatrix} \qquad C = \begin{pmatrix} 1 & 0 & 0 \\ 0 & 1 & 0 \end{pmatrix}$$

The zero dynamics of the original system (2), obtained by setting $x = 0$ in Eq. (12), are given by the trajectories of the controlled system:

$$\dot{z} = F(\mu)z + G(\mu)u_a \qquad y_a = H(\mu, x_{\text{rg}})z \tag{13}$$

where the eigenvalues of $F(\mu)$ coincide with the transmission zeros of the multivariable transfer function of system (2) between u_b and y. It can be verified that the zero dynamics (13) comprise the flexible dynamics and the rigid-body pitch dynamics. Consequently, $F(\mu)$ possesses three pairs of complex conjugate eigenvalues with $\text{Re}[\lambda] < 0$ (due to the flexible states) and a pair of real eigenvalues (due to the pitch dynamics) located almost symmetrically with respect to the imaginary axis. The pair $(F(\mu), G(\mu))$ is controllable for all $\mu \in \mathcal{P}$, and the pair $(H(\mu, x_{\text{rg}}), F(\mu))$ is observable if the output map is selected appropriately, as discussed in the following section. The pole-zero map of system (13) is shown in Fig. 7a for the rate gyro located at $x_{\text{rg}} = 1$ ft. Because the poles of the zero dynamics are transmission zeros of system (12), controlling altitude and velocity by means of the fuel-to-air ratio and the elevator surface deflection results in a nonminimum-phase system. The structure of system (12) suggests the following design strategy: First find a dynamic controller for the zero dynamics (13) that renders the compensated system to be robustly of minimum phase with respect to the I/O pair (u_b, y), then design a controller using measurements of the regulated output to achieve output tracking.

A. Robust Stabilization of the Zero Dynamics

The first task is to design an output-feedback controller for the zero dynamics that provide robust stability over the range of operating conditions. A closer inspection of the structure of Eq. (13) reveals that this system has a relative degree of 1 and is a weakly nonminimum-phase system; that is, all zeros are in the closed left-half-plane, except for a simple zero at the origin. This is seen from the pole-zero map in Fig. 7a. It is clear that any static negative output feedback $u_a = -K_a y_a$ $(K_a > 0)$ will result in an unstable closed loop, because the right-hand pole will migrate toward the zero at the origin. However, the positive feedback interconnection with a simple dynamic compensator of the form

$$\mathcal{K}_0(s) = -k_0 \frac{s + b_0}{s - a_0} \qquad k_0 > 0 \qquad b_0 > 0 \qquad a_0 > 0 \tag{14}$$

results in a stable closed-loop system for a given value of μ if the parameters a_0 and b_0 are chosen smaller than the magnitude of the unstable pole and k_0 is sufficiently large. For this choice of a stabilizing controller, the selection of the location of the rate gyro is performed on the basis of a simple criterion: namely, maintaining a desirable pole-zero structure for all possible values of μ to achieve robust stabilization. Here, the most desirable situation is attained if, after compensation using Eq. (14), the angles of departure of the root

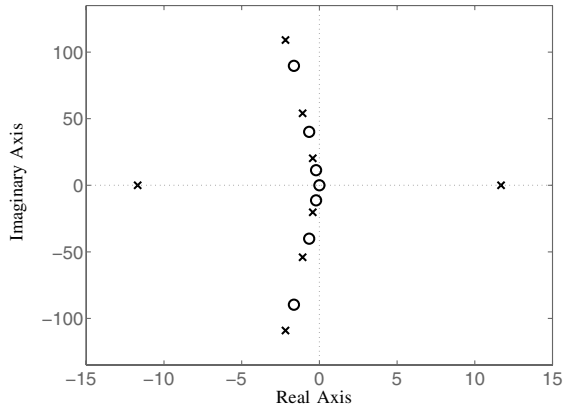

a) Pole-zero map of the uncompensated zero dynamics, $\mu = \mu_0$, $x_{\text{rg}} = 1$ft

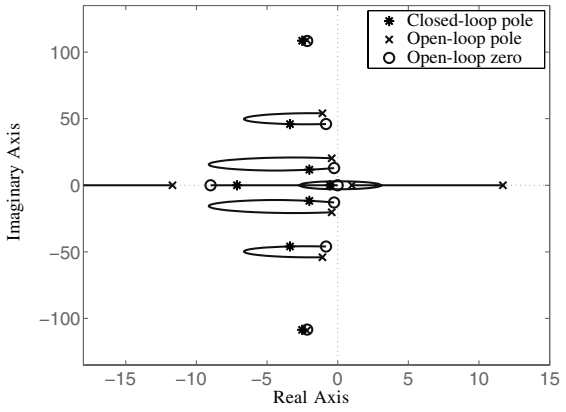

b) Root locus of the compensated zero dynamics, $\mu = \mu_0$, $x_{\text{rg}} = 26$ft

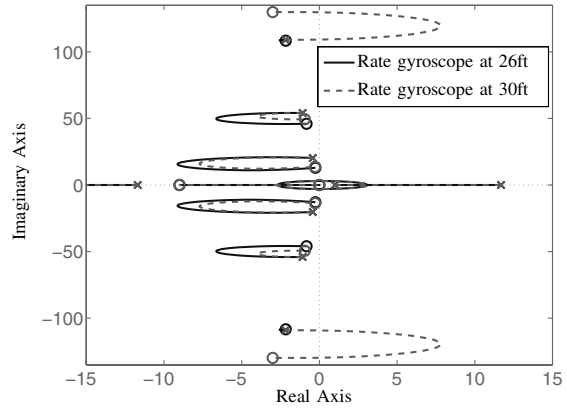

c) Root loci of the compensated zero dynamics; rate gyro placed at $x_{\text{rg}} = 26$ ft (solid) and $x_{\text{rg}} = 30$ ft (dashed), $\mu = \mu_0$

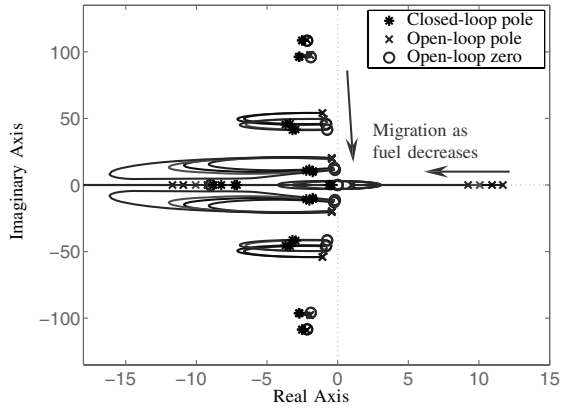

d) Root loci of the compensated zero dynamics for variations in fuel level and trim condition

Fig. 7 Pole-zero maps and root loci of the uncompensated and compensated zero dynamics.

loci originating from the complex poles remain toward the left for all $\mu \in \mathcal{P}$. If this is verified, then there exists a selection of the controller parameters that provides robust stabilization. Moving the sensor away from the nose of the vehicle causes the complex zeros to migrate away from the real axis and to modify the angle of departure. The root locus of the compensated system using the controller (14) and sensor located at $x_{\text{rg}} = 26$ ft are shown in Fig. 7b for the nominal case $\mu = \mu_0$, and the parameters of the auxiliary controller are as follows: $k_0 = 2$, $b_0 = 9$, and $a_0 = 1$. Figure 7c illustrates the difference between the root loci obtained under the same compensator when x_s is changed from 26 to 30 ft from the nose. Finally, Fig. 7d shows an example of the variation of the root loci obtained when the fuel level is varied from 50 to 90% and the trim conditions are taken within the range of $7846 \leq V_t^\star \leq 8846$ ft/s and $85,000 \leq h^\star \leq 95,000$ ft, respectively. Note that the same controller stabilizes the system in all configurations. Finally, the Bode plots of the loop gain of the zero dynamics, before and after compensation, are shown in Fig. 8. It can be verified that at nominal conditions, the compensated zero dynamics has a gain margin of about 9 dB and a phase margin greater than 50 deg.

B. Internal Model-Based Control

The state-space realization of the robust compensator $\mathcal{K}_0(s)$, given by the system

$$\dot{\xi}_0 = a_0\xi_0 + (b_0 + a_0)y_a \qquad u_a = -k_0\xi_0 - k_0 y_a \tag{15}$$

with state $\xi_0 \in \mathbb{R}$, is then incorporated in the zero dynamics, yielding the augmented system:

$$\begin{aligned} \dot{z}^a &= F^a(\mu)z^a + J_1^a(\mu)x \\ \dot{x} &= A^a(\mu)x + J_2^a(\mu)z^a + B(\mu)u_b \\ y &= Cx \end{aligned} \tag{16}$$

where $z^a = (\xi_0, z^T)^T \in \mathbb{R}^9$, and the system matrices are defined appropriately. Note that $A^a(\mu)$ has the same structure as $A(\mu)$. Because, by construction, the eigenvalues of $F^a(\mu)$ are in the left-half plane for all $\mu \in \mathcal{P}$, a viable strategy to control the overall system (16) is to use feedback from state x only. Recall that state x is composed of the regulated output (altitude and velocity), plus the time derivative of the altitude, $\dot{h}$. Before proceeding with the design of the control law, a preliminary dynamic transformation is employed to avoid the need to differentiate the measurement of the altitude. To this end, the dynamics of Eq. (16) are augmented with the stable filter:

$$\dot{\xi}_1 = -\lambda\xi_1 + \delta_e \tag{17}$$

where $\lambda > 0$ is a design parameter. Then by applying the results of Sec. 11.3 in [48], it is possible to show that there exists a change of coordinates $(z^a, x, \xi_1) \to (\bar{z}^a, \bar{x})$, where $\bar{z}^a \in \mathbb{R}^{10}$ and $\bar{x} = (V_t - V_t^\star, h - h^\star, \xi_1)^T$, yielding the augmented system:

$$\begin{aligned} \dot{\bar{z}}^a &= \bar{F}^a(\mu)\bar{z}^a + \bar{J}_1^a(\mu)y \\ \dot{\bar{x}} &= \bar{A}^a(\mu)\bar{x} + \bar{J}_2^a(\mu)\bar{z}^a + \bar{B}^a(\mu)u_{\text{rb}} \\ y &= C\bar{x} \end{aligned} \tag{18}$$

In Eq. (18), the matrix $\bar{F}^a(\mu)$ is Hurwitz for any $\mu \in \mathcal{P}$, because its eigenvalues are those of $F^a(\mu)$ plus the eigenvalue at $-\lambda$ of the stable filter. The matrices $\bar{A}^a$, $\bar{B}^a$, and $\bar{J}_2^a$ have the form

$$\bar{A}^a(\mu) = \begin{pmatrix} \bar{a}_{11}^a(\mu) & \bar{a}_{12}^a(\mu) & \bar{a}_{13}^a(\mu) \\ \bar{a}_{21}^a(\mu) & \bar{a}_{22}^a(\mu) & \bar{a}_{23}^a(\mu) \\ 0 & 0 & -\lambda \end{pmatrix}$$

$$\bar{B}^a(\mu) = \begin{pmatrix} b_{11}(\mu) & b_{12}(\mu) \\ 0 & 0 \\ 0 & 1 \end{pmatrix} \qquad \bar{J}_2^a(\mu) = \begin{pmatrix} \bar{J}_{21}^a(\mu) \\ \bar{J}_{22}^a(\mu) \\ 0 \end{pmatrix}$$

with $\bar{a}_{23}^a(\mu) > 0$ for all $\mu \in \mathcal{P}$. For convenience of notation, from now on we will explicitly use the components of the vectors u_b, y, and $\bar{x}$, denoted, respectively, as $u_b = (u_1, u_2)^T$, $y = (y_1, y_2)^T$, and $\bar{x} = (x_1, x_2, \xi_1)^T$, in lieu of their physical meaning.

The triangular structure of system (18) suggests a hierarchical approach to control design. Specifically, the inner $(x_2, \xi_1)^T$ subsystem corresponding to the extended altitude dynamics will be controlled via u_2 on a faster timescale than with the outer x_1 subsystem (the velocity dynamics), which will be controlled using u_1. The zero dynamics of system (18) with respect to the I/O pair (u_1, y_1) is given by the controlled system:

$$\begin{aligned} \dot{\bar{z}}^a &= \bar{F}^a(\mu)\bar{z}^a + \bar{J}_{12}^a(\mu)x_2 \\ \dot{x}_2 &= \bar{J}_{22}^a(\mu)\bar{z}^a + \bar{a}_{22}^a(\mu)x_2 + \bar{a}_{23}^a(\mu)\xi_1 \\ \dot{\xi}_1 &= -\lambda\xi_1 + u_2 \\ y_2 &= x_2 \end{aligned} \tag{19}$$

which, by inspection, has a relative degree of 2 with respect to the I/O pair (u_2, y_2), transmission zeros in the left-half plane [corresponding to the eigenvalues of $\bar{F}^a(\mu)$], and state $(x_2, \xi_1)^T$ available for feedback. Therefore, it is possible to design a robust controller using feedback from the partial state $(x_2, \xi_1)^T$ that achieves tracking for the inner loop (19). This controller will be termed $\mathcal{K}_2$. Once a robust controller for Eq. (19) has been designed, we are left to design a tracking controller $\mathcal{K}_1$ for the outer loop, which is a relative-degree-of-1 system with input u_1, output x_1, and stabilized zero dynamics. The approach is shown schematically in Fig. 9. The two controllers will be designed using internal model control [22,23,26]. The controllers embed an internal model of the reference trajectory generator (7) to achieve robust tracking in the presence of parameter uncertainty, whereas the augmented system is robustly stabilized using dynamic feedback from the regulated output y.

For the inner-loop regulator, augment system (19) with the reference model for r_2 in Eq. (7), and define the tracking error as $e_2 = x_2 - r_2$. The goal of the controller $\mathcal{K}_2$ is to enforce (by dynamic

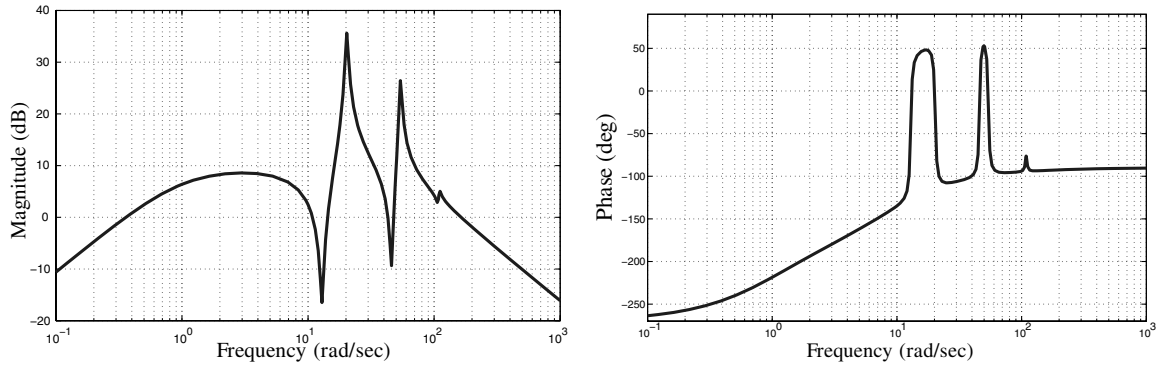

a) Compensated system, magnitude plot **b) Compensated system, phase plot**

Fig. 8 Bode plots of the loop gain of the zero dynamics, after compensation; rate gyro located at $x_{\text{rg}} = 26$ ft; nominal fuel level.

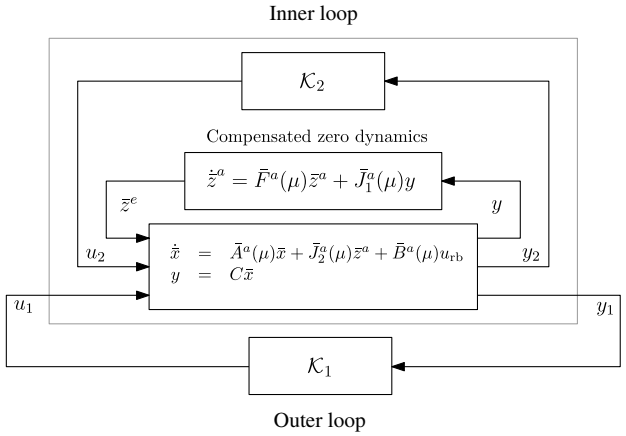

Fig. 9 Inner-loop and outer-loop control with compensated zero dynamics.

feedback) an invariant subspace for the augmented system in which the tracking error is identically zero and to render that subspace globally attractive. Furthermore, the controller should induce a timescale separation between the inner-loop and the outer-loop dynamics to facilitate the design of $\mathcal{K}_1$. Assuming that the spectra of S_2 and $\bar{F}^a(\mu)$ are separated, there exists a unique solution $\Pi_2(\mu)$ of the Sylvester equation:

$$\Pi_2(\mu)S_2 = \bar{F}^a(\mu)\Pi_2(\mu) + \bar{J}_{12}^e(\mu)Q_2$$

The change of coordinates $e_2 = x_2 - r_2$ and $\tilde{z}^a = \bar{z}^a - \Pi_2(\mu)w_2$ yields the error system:

$$\begin{aligned}
\dot{w}_2 &= S_2 w_2 \\
\dot{\tilde{z}}^a &= \bar{F}^a(\mu)\tilde{z}^a + \bar{J}_{12}^a(\mu)e_2 \\
\dot{e}_2 &= \bar{J}_{22}^a(\mu)\tilde{z}^a + \bar{a}_{22}^a(\mu)e_2 + \bar{a}_{23}^a(\mu)[\xi_1 - R_2(\mu)w] \\
\dot{\xi}_1 &= -\lambda\xi_1 + u_2
\end{aligned} \tag{20}$$

where

$$R_2(\mu) = \frac{1}{\bar{a}_{23}^a(\mu)}[\bar{J}_{22}^a(\mu)\Pi_2(\mu) + \bar{a}_{22}^a(\mu)Q_2 - Q_2S_2]$$

For system (20) to have an equilibrium at $\tilde{z}^a = 0$ and $e_2 = 0$ (corresponding to perfect tracking for y_2), the state $\xi_1(t)$ must be steered to the steady-state trajectory $\xi_1^\star(t) = R_2(\mu)w(t)$. The problem is that $\xi_1^\star(t)$ is not known a priori because it depends on μ and thus must be reconstructed by the controller. This is achieved by means of the internal model principle [49,50].

Assume, without loss of generality, that the pair $(R_2(\mu), S_2)$ is observable for all $\mu \in \mathcal{P}$. Then the given pair is equivalent to the pair $(Q_2, \bar{S}_2)$, where $\bar{S}_2$ is in controller canonical form. It is easy to check that the pairs $(R_2(\mu), S_2)$ and $(Q_2, \bar{S}_2)$ are related through the similarity transformation:

$$S_2 = \Theta_2^{-1}(\mu)\bar{S}_2\Theta_2(\mu) \qquad R_2(\mu) = Q_2\Theta_2(\mu)$$

where $\Theta_2(\mu)$ is the observability matrix of $(R_2(\mu), S_2)$. Because the pair Q_2 and $\bar{S}_2$ is independent of the uncertain parameter μ, it can be used to build an *internal model* of the unknown steady-state trajectory $\xi_1^\star(t)$. The construction of the internal model is accomplished by using a novel formulation of the methodology described in Sec. 1.5 of [26]. In the solution presented here, the choice of the controller gains follows a simple and intuitive procedure that corresponds to enforcing a suitable timescale separation among the controlled variables in such a way that standard arguments in singular perturbations apply for stability analysis.

Let $\rho > 0$ be an adjustable gain parameter, and define the scaling parameter $\varepsilon = 1/\rho$. Let (Σ_2, Ξ_2) be the pair in controller form:

$$\Sigma_2 = \begin{pmatrix} 0 & 1 & 0 \\ 0 & 0 & 1 \\ -\sigma_0 & -\sigma_1 & -\sigma_2 \end{pmatrix} \qquad \Xi_2 = \begin{pmatrix} 0 \\ 0 \\ 1 \end{pmatrix} \tag{21}$$

where the roots of the characteristic polynomial of Σ_2 are chosen arbitrarily in the left-half plane, away from the eigenvalues of $\bar{S}_2$. Then for any $\rho > 0$, there exists a unique nonsingular solution $M_2(\rho)$ of the Sylvester equation:

$$M_2(\rho)\bar{S}_2 = \rho\Sigma_2 M_2(\rho) + \Xi_2 Q_2 \tag{22}$$

Let $\Psi_2(\varepsilon) = Q_2 M_2^{-1}(\rho)\rho^{-1}$. It is readily seen that $\rho\Psi(\varepsilon)$ is the unique feedback matrix that assigns the eigenvalues of $\bar{S}_2$ to the pair $(\rho\Sigma_2, \Xi_2)$; therefore, $\Sigma_2(\varepsilon)$ can easily be computed as

$$\Psi_2(\varepsilon) = \begin{pmatrix} \sigma_0 & \sigma_1 - \varepsilon\omega_n^2 & \sigma_2 - 2\varepsilon\zeta\omega_n \end{pmatrix} \tag{23}$$

Note that $\Psi_2(\varepsilon) = \mathcal{O}(1)$. Following Sec. 1.5 of [26], a candidate internal model for the steady-state trajectory $\xi_1^\star(t)$ is constructed as the dynamic system:

$$\dot{\xi}_2 = \rho\Sigma_2\xi_2 + \Xi_2\xi_1 \qquad \upsilon = \rho\Psi_2(\varepsilon)\xi_2 \tag{24}$$

Augmenting system (20) with the internal model (24), changing coordinates as

$$\begin{aligned}
\tilde{\xi}_1 &= \xi_1 - \rho\Psi_2(\varepsilon)\xi_2 \\
\tilde{\xi}_2 &:= \xi_2 - M_2(\rho)\Theta_2^{-1}(\mu)w - \frac{1}{\bar{a}_{23}^a(\mu)}\Xi_2 e_2
\end{aligned}$$

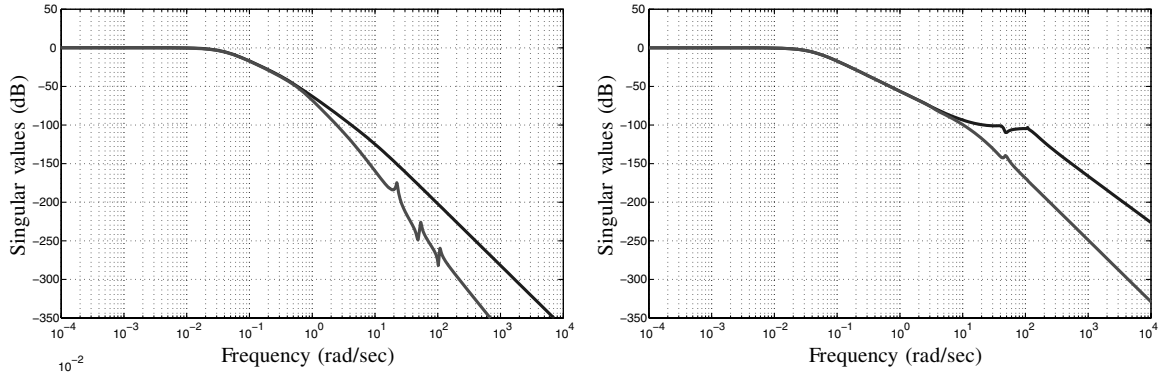

a) Baseline controller **b) Internal model controller**

Fig. 10 Singular-value Bode plot of the closed-loop transfer-function matrix from *r* to *y*; nominal operating conditions.

and rearranging terms, it becomes apparent that the control u_2 should be selected as

$$u_2 = [\lambda + \rho\Psi_2(\varepsilon)\Xi_2]\xi_1 + \rho^2\Psi_2(\varepsilon)\Sigma_2\xi_2 - \rho k_{22}[\tilde{\xi}_1 + k_{21}e_2] \quad (25)$$

where $k_2 = (k_{21}, k_{22})^T$ is a vector of positive gain parameters. The control law in Eq. (25) has the structure of a proportional/derivative control with feedforward action, where k_{22} and $k_{22}k_{21}$ are the gains of the derivative and the proportional feedback, respectively. The feedforward term creates the required equilibrium at the origin by removing known terms that do not vanish at $e_2 = 0$, whereas the proportional/derivative feedback stabilizes the equilibrium robustly with respect to μ.

Equation (25) yields the augmented closed-loop dynamics in the standard singular-perturbation form [51]:

$$\begin{aligned} \dot{\tilde{z}}^a &= \bar{F}^a(\mu)\tilde{z}^a + \bar{J}^a_{12}(\mu)C_2\chi_2 \\ \varepsilon\dot{\chi}_2 &= A_2(\mu, \varepsilon, k_2)\chi_2 + \varepsilon B_2(\mu)\tilde{z}^a \end{aligned} \quad (26)$$

where $\chi_2 = (e_2, \tilde{\xi}_1^T, \tilde{\xi}_2^T)^T$ and, in particular,

$$A_2(\mu, \varepsilon, k_2) = \begin{pmatrix} \varepsilon\bar{a}^a_{22}(\mu) + \Psi_2(\varepsilon)\Xi_2 & \varepsilon\bar{a}^a_{23}(\mu) & \bar{a}^a_{23}(\mu)\Psi_2(\varepsilon) \\ -k_{21}k_{22} & -k_{22} & 0 \\ \frac{1}{\bar{a}^a_{23}(\mu)}[\Sigma_2\Xi_2 - \varepsilon\bar{a}^a_{22}(\mu)\Xi_2] & 0 & \Sigma_2 \end{pmatrix}$$

The following result follows from arguments similar to those in Lemma 1.5.4 of [26]; therefore, its proof is omitted.

Proposition 1: There exist numbers $k^\star_{21}, k^\star_{22} > 0$ such that for any given $k_{21} \geq k^\star_{21}$ and $k_{22} \geq k^\star_{22}$, the matrix $A_2(\mu, \varepsilon, k_2)$ is Hurwitz for all $\mu \in \mathcal{P}$ and all $\varepsilon \in (0, 1]$.

Once values $k_{21} \geq k^\star_{21}$ and $k_{22} \geq k^\star_{22}$ have been fixed, the occurrence of k_2 from the arguments of $A_2(\cdot)$ is removed to simplify the notation and to emphasize the fact that $A_2(\mu, \varepsilon)$ is now a Hurwitz matrix. The next proposition follows directly from Lemma 2.1 in [51]:

Proposition 2: There exists $0 < \varepsilon^\star \leq 1$ such that for all $\varepsilon \in (0, \varepsilon^\star]$, there exists a solution $L(\mu, \varepsilon)$ of the quadratic matrix equation:

$$\begin{aligned} &B_2(\mu) + A_2(\mu, \varepsilon)L(\mu, \varepsilon) \\ &\quad - \varepsilon L(\mu, \varepsilon)\bar{F}^a(\mu) - \varepsilon L(\mu, \varepsilon)\bar{J}^a_{12}(\mu)C_2L(\mu, \varepsilon) \end{aligned}$$

which is approximated as

$$\begin{aligned} L(\mu, \varepsilon) &= -A_2^{-1}(\mu, \varepsilon)B_2(\mu) \\ &\quad - \varepsilon A_2^{-1}(\mu, \varepsilon)B_2(\mu)[\bar{F}^a(\mu) - \bar{J}^a_{12}(\mu)C_2A_2^{-1}(\mu, \varepsilon)B_2(\mu)] + \mathcal{O}(\varepsilon^2) \end{aligned}$$

Note that because the matrix $B_2(\mu)$ appears in Eq. (26) scaled by ε, the change of coordinates required to bring Eq. (26) into the so-called standard actuator form is given by

$$\tilde{\chi}_2 = \chi_2 - \varepsilon L(\mu, \varepsilon)\tilde{z}^a$$

where $\varepsilon \in (0, \varepsilon^\star]$. This transformation yields the singularly perturbed system

$$\begin{aligned} \dot{\tilde{z}}^a &= [\bar{F}^a(\mu, \varepsilon) = \bar{F}^a(\mu) + \varepsilon\bar{J}^a_{12}(\mu)C_2L(\mu, \varepsilon)]\tilde{z}^a + \bar{J}^a_{12}(\mu)C_2\tilde{\chi}_2 \\ \varepsilon\dot{\tilde{\chi}}_2 &= [A_2(\mu, \varepsilon) - \varepsilon^2 L(\mu, \varepsilon)\bar{J}^a_{12}(\mu)C_2]\tilde{\chi}_2 \end{aligned} \quad (27)$$

for which it is now obvious to conclude the following:

Proposition 3: There exists $\varepsilon^{\star\star} \in (0, \varepsilon^\star]$ such that system (27) is asymptotically stable for all $(\mu, \varepsilon) \in \mathcal{P} \times (0, \varepsilon^{\star\star}]$.

The result of the design process is summarized in the following proposition:

Proposition 4: Consider the dynamic error-feedback controller

$$\begin{aligned} \dot{\xi}_1 &= -\lambda\xi_1 + u_2 \\ \dot{\xi}_2 &= \rho\Sigma_2\xi_2 + \Xi_2\xi_1 \\ u_2 &= [\lambda + \rho\Psi_2(\varepsilon)\Xi_2 - \rho k_2]\xi_1 \\ &\quad + \rho^2\Psi_2(\varepsilon)[k_{22}I + \Sigma_2]\xi_2 - \rho k_{21}k_{22}e_2 \end{aligned} \quad (28)$$

where $\lambda > 0, k_{21} > 0, k_{22} > 0$, and $\rho > 0$ are tunable gain parameters, and Σ_2, Ξ_2, and $\Psi_2(\varepsilon)$ are given in Eqs. (21) and (23), respectively. Choose $k_{21} \geq k^\star_{21}$ *and* $k_{22} \geq k^\star_{22}$ according to Proposition 1. Then there exists $\rho^\star \geq 1$ such that for all $\rho \geq \rho^\star$, the controller (28) applied to system (19) achieves boundedness of all trajectories and asymptotic regulation of the tracking error $e_2(t)$.

The design of the outer-loop regulator $\mathcal{K}_1$ is accomplished on the basis of the boundary-layer system, similar to that for $\mathcal{K}_2$. The boundary-layer system is obtained by deriving the expression of Eq. (27), keeping x_1 in the equations, and setting $\varepsilon = 0$. In the boundary layer, χ_2 becomes a linear function of x_1, allowing a drastic simplification for the design of $\mathcal{K}_1$. Details are skipped for brevity. The regulator $\mathcal{K}_1$ is implemented as the system

$$\dot{\xi}_3 = \Sigma_1\xi_3 + \Xi_1 e_1 \qquad u_1 = -k_1 e_1 + \Psi_1\xi_3 \quad (29)$$

where $e_1 = y_1 - r_1$ is the tracking error, $k_1 > 0$ is a design parameter, and the triplet $(\Sigma_1, \Xi_1, \Psi_1)$ in controller companion form plays the same role as $(\Sigma_2, \Xi_2, \Psi_2)$. In particular, Σ_1 is Hurwitz and Ψ_1 is the feedback matrix that assigns the eigenvalues of S_1 to (Σ_1, Ξ_1).

Although the structure of the overall regulator may appear to be a bit intricate at a first glance, the actual tuning of the controller parameters is simple and intuitive and follows the systematic sequential procedure summarized next:

1) Choose the location of the rate gyro x_{rg} and the gains k_0, a_0, and b_0 such that the compensated zero dynamics (13–15) are asymptotically stable for all $\mu \in \mathcal{P}$.

2) Fix $\lambda > 0$, and choose the Hurwitz matrices Σ_1 and Σ_2 such that their spectra are separated from those of S_1 and S_2, respectively.

3) Fix $\rho = 1$, and compute $k^\star_{21}$ and $k^\star_{22}$ as the smallest such values for which the matrix $A_2(\mu, 1, k_2)$ is Hurwitz for all $\mu \in \mathcal{P}$. Fix values $k_{21} \geq k^\star_{21}$ and $k_{22} \geq k^\star_{22}$.

4) Select $\rho > 1$ such that system (26) is asymptotically stable for all perturbed models.

5) Choose $k_1 > 0$ large enough such that the closed-loop system is asymptotically stable. The gains and design parameters of the controllers $\mathcal{K}_1$ and $\mathcal{K}_2$ employed for the linearized nominal model considered in this study are as follows: $\lambda = 0.05$, $k_1 = 1.001$, $k_{21} = 10$, and $k_{22} = 10$; eigenvalues of Σ_1 are

$$(-1, \ -3.4, \ -3.68) \times 10^{-4}$$

and eigenvalues of Σ_2 are

$$(-0.8, \ -2.672, \ -2.944) \times 10^{-4}$$

The design parameters of the controller $\mathcal{K}_0$ are described in Sec. IV.A.

C. Simulation Results

The robust internal model-based controller was simulated in a closed loop with the nonlinear model (1). Figure 10b shows the Bode plot of the singular values of the closed-loop transfer function from the reference to the regulated output obtained with the robust controller. In all simulations, the nonlinear plant model was initialized at the trim condition given in Table 2. The reference to be tracked is the same used for the baseline controller. Extensive simulations were performed changing the plant parameters to account for uncertainty in the flexible dynamics produced by variations of the fuel level. Although the performance of the robust controller is comparable with that of the baseline controller for nominal fuel conditions, it provides stable tracking for a much wider

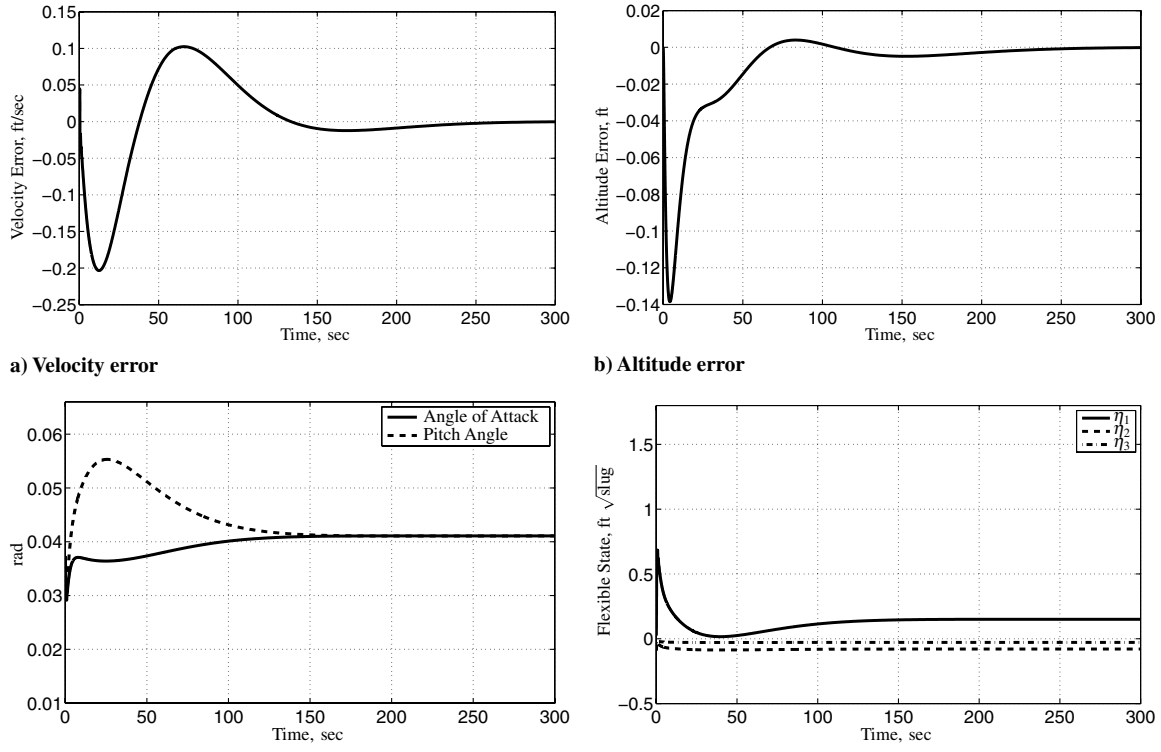

a) Velocity error **b) Altitude error**

c) Angle of attack, pitch angle **d) Flexible states**

Fig. 11 Simulation results for the robust servomechanism controller; nonlinear simulations; 30% fuel level.

range of operating conditions. Figures 11a, 12a, and 13a and Figs. 11b, 12b, and 13b show, respectively, the tracking error for velocity and altitude obtained with 30, 50 (nominal), and 70% fuel conditions. It can be seen that the tracking error remains very well-behaved in all cases and converges to zero asymptotically. Figures 11c, 12c, and 13c and Figs. 11d, 12d, and 13d show that the controller maintains a stable and damped behavior for the pitch angle, the angle of attack, and the flexible states for all considered fuel levels within the range 30–70%. In particular, the second and third bending modes are not excited in closed-loop operation,

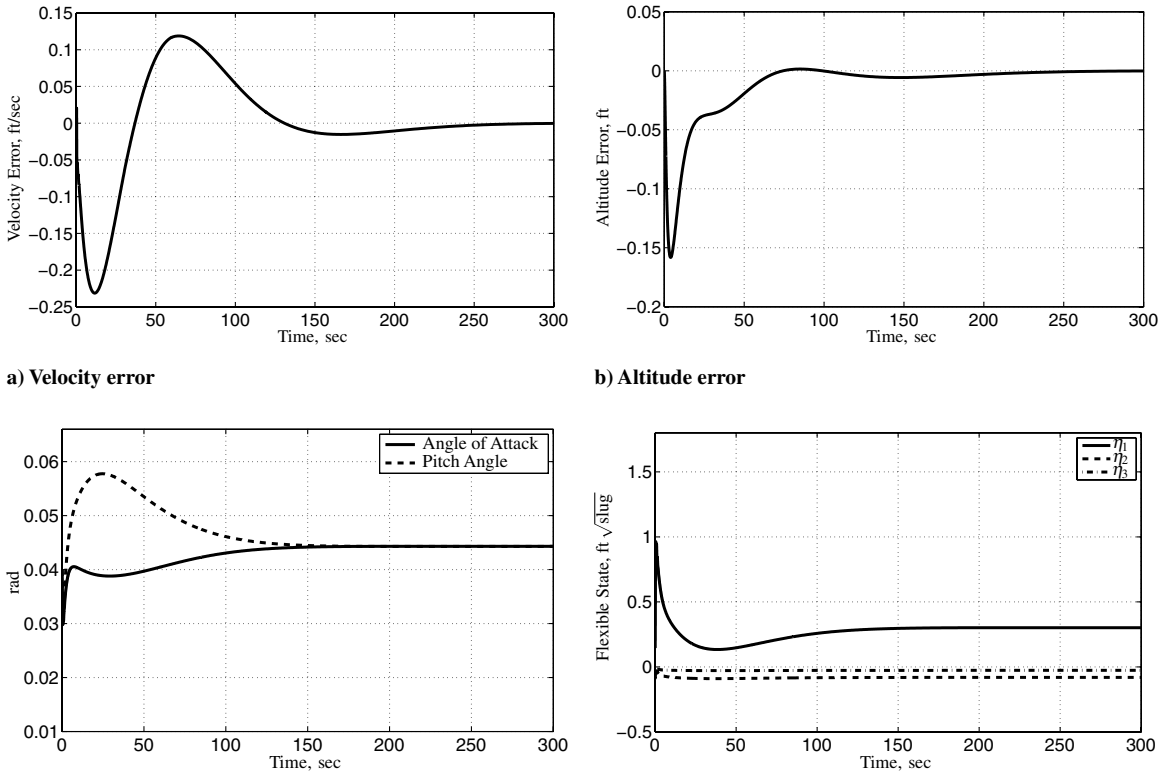

a) Velocity error **b) Altitude error**

c) Angle of attack, pitch angle **d) Flexible states**

Fig. 12 Simulation results for the robust servomechanism controller; nonlinear simulations; 50% fuel level.

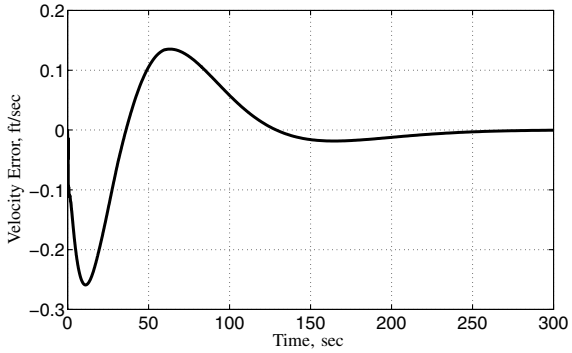

a) Velocity error

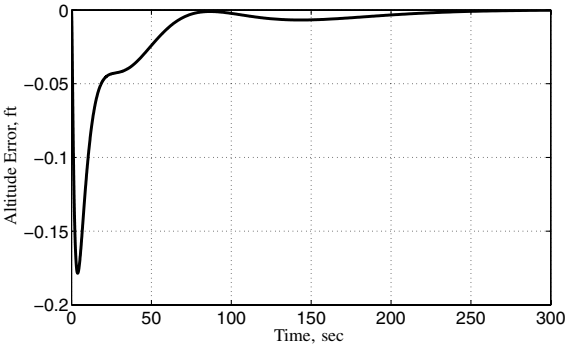

b) Altitude error

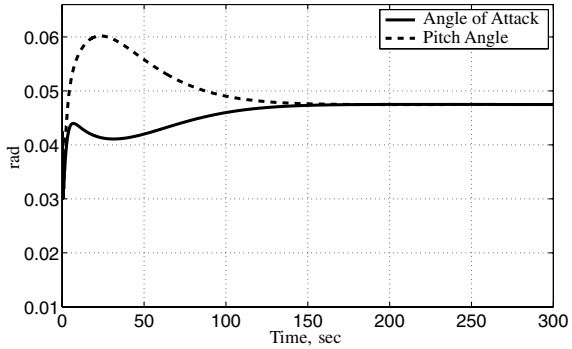

c) Angle of attack, pitch angle

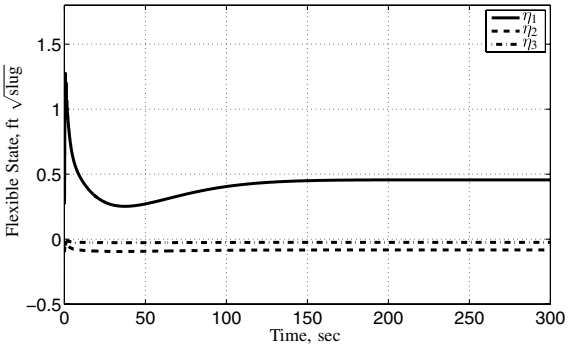

d) Flexible states

Fig. 13 Simulation results for the robust servomechanism controller; 70% fuel level.

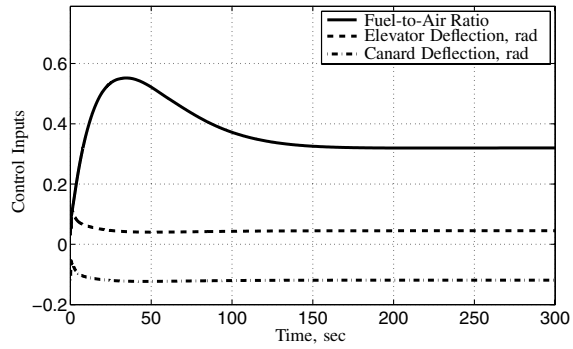

a) Control input, 30% fuel level

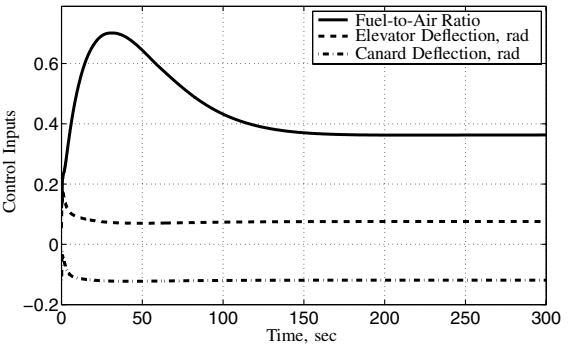

b) Control input, 70% fuel level

Fig. 14 Control inputs $\phi(t)$, $\delta_e(t)$, and $\delta_c(t)$; nonlinear simulations.

showing that the spillover effect [52] is avoided. Finally, the control signals, shown in Fig. 14 for 30 and 70% fuel levels, remain well within the magnitude limits, and the rate limitations do not compromise the stability of the loop.

V. Conclusions

Robustness against model uncertainty is a fundamental issue when designing baseline output-feedback controllers for generic air-breathing hypersonic vehicle models. Poor closed-loop performance exhibited by observer-based controllers in simulations with a nonlinear model of the longitudinal vehicle dynamics, even in the face of moderate parameter variations, warranted the exploration of methodologies alternative to certainty-equivalence design. In this paper, an approach to output-feedback design that is robust to variations in vehicle mass due to fuel consumption was proposed and was validated in nonlinear simulations. As mentioned, variations due to fuel consumption should be interpreted here as being representative of general parametric uncertainties affecting the model dynamics. Among the merits and drawbacks of the approach presented lies the obvious fact that robust servomechanism design does not rely on state observation and thus is not influenced by the accuracy of state estimates. A possible drawback is constituted by the fact that the design is partially based on high-gain feedback, which may have the potential to excite the flexible dynamics. This limitation, however, can be avoided in many cases by a judicious choice of the parameters of the internal model and the stabilizer of the zero dynamics and by stability augmentation. As seen in the discussion in Sec. IV.C, the values of the gains obtained for the synthesis presented in this paper are indeed of the same order or smaller than the gains obtained with the baseline design, and the closed-loop bandwidth was verified to remain below the natural frequencies of the flexible dynamics. In this regard, an important aspect to consider when comparing the robust internal model-based controller with the baseline design is the complexity of the tuning of the gains. The non-observer-based controller provides a much

simpler approach for the synthesis of the compensator, because the zero dynamics are stabilized at the first step of the design process, and robust compensation is achieved for a lower-order model than with the system considered in the observer design. For the latter case, the design of the weighting functions of the LQR/LQE optimization may become quite involved. There is also a sharp contrast between the strategies for selecting the output maps. The controller based on robust servomechanism theory uses only one rate gyro with a simple allocation strategy, whereas the other controller requires one to choose the location of two sensors on the basis of observability analysis.

Though the approach presented here provides robust performance under significant changes in flight conditions and fuel level, it must be kept in mind that the underlying strategy remains based on linear control. Although it is unreasonable to expect an acceptable level performance to be maintained over the entire flight envelope (i.e., supersonic, transonic, and subsonic flight) or a very large set of trim conditions, the proposed controller stands out as a viable candidate for a robust gain-scheduling control design. As a matter of fact, the capability of the robust controller to provide stable tracking for an enlarged subset of operating conditions presents a clear advantage over the baseline controller for implementation in a gain-scheduling control architecture, because the need for interpolation over a fine grid of operating conditions is avoided. In addition, robustness with respect to the model parameters may provide a viable and simpler alternative to strategies based on a continuous update of the controller gains, such as those employed in adaptive [11,13] or linear parameter-varying controllers [41], in which the assessment of robustness metrics and stability margins may be difficult.

Acknowledgments

This work was supported by the U.S. Air Force Research Laboratories Air Vehicles Directorate, U.S. Air Force Office of Scientific Research, and the Dayton Area Graduate Studies Institute through the Collaborative Center of Control Science at The Ohio State University (contract F33615-01-2-3154).

References

[1] Chavez, F., and Schmidt, D., "Analytical Aeropropulsive/Aeroelastic Hypersonic-Vehicle Model with Dynamic Analysis," *Journal of Guidance, Control, and Dynamics*, Vol. 17, No. 6, 1994, pp. 1308–19.

[2] Bilimoria, K., and Schmidt, D., "Integrated Development of the Equations of Motion for Elastic Hypersonic Flight Vehicles," *Journal of Guidance, Control, and Dynamics*, Vol. 18, No. 1, 1995, pp. 73–81.

[3] Cockrell, C. Jr, Engelund, W., Bittner, R., Jentink, T., Dilley, A., and Frendi, A., "Integrated Aeropropulsive Computational Fluid Dynamics Methodology for the Hyper-X Flight Experiment," *Journal of Spacecraft and Rockets*, Vol. 38, No. 6, 2001, pp. 836–843.

[4] Bolender, M. A., and Doman, D. B., "A Nonlinear Longitudinal Dynamical Model of an Airbreathing Hypersonic Vehicle," *Journal of Spacecraft and Rockets*, Vol. 44, No. 2, 2007, pp. 374–387. doi:10.2514/1.23370

[5] Friedmann, P., and McNamara, J., "Aeroelastic and Aerothermoelastic Analysis of Hypersonic Vehicles: Current Status and Future Trends," AIAA Paper 2007-2013, Apr. 2007.

[6] Chavez, F., and Schmidt, D., "Uncertainty Modeling for Multivariable-Control Robustness Analysis of Elastic High-Speed Vehicles," *Journal of Guidance, Control, and Dynamics*, Vol. 22, No. 1, 1999, pp. 87–95.

[7] Bolender, M., and Doman, D., "Modeling Unsteady Heating Effects on the Structural Dynamics of a Hypersonic Vehicle," AIAA Paper 2006-6646, Aug. 2006.

[8] Williams, T., Bolender, M. A., Doman, D. B., and Morataya, O., "An Aerothermal Flexible Mode Analysis of a Hypersonic Vehicle," AIAA Paper 2006-6647, Aug. 2006.

[9] Mirmirani, M., Wu, C., Clark, A., Choi, S., and Colgren, R., "Modeling for Control of a Generic Airbreathing Hypersonic Vehicle," AIAA Paper 2005-6256, Aug. 2005.

[10] Fidan, B., Mirmirani, M., and Ioannou, P., "Flight Dynamics and Control of Airbreathing Hypersonic Vehicles: Review and New Directions," AIAA Paper 2003-7081, Dec. 2003.

[11] Fidan, B., Kuipers, M., Ioannou, P., and Mirmirani, M., "Longitudinal Motion Control of Air-Breathing Hypersonic Vehicles Based on Time-Varying Models," AIAA Paper 2006-8074, Nov. 2006.

[12] Huo, Y., Mirmirani, M., Ioannou, P., and Kuipers, M., "Altitude and Velocity Tracking Control for an Airbreathing Hypersonic Cruise Vehicle," AIAA Paper 2006-6695, Aug. 2006.

[13] Kuipers, M., Mirmirani, M., Ioannou, P., and Huo, Y., "Adaptive Control of an Aeroelastic Airbreath-ing Hypersonic Cruise Vehicle," AIAA Paper 2007-6326, Aug. 2007.

[14] Groves, K. P., Sigthorsson, D. O., Serrani, A., Yurkovich, S., Bolender, M. A., and Doman, D. B., "Reference Command Tracking for a Linearized Model of an Airbreathing Hypersonic Vechicle," AIAA Paper 2005-6144, Aug. 2005.

[15] Sigthorsson, D. O., Serrani, A., Yurkovich, S., Bolender, M. A., and Doman, D. B., "Tracking Control for an Overactuated Hypersonic Airbreathing Vehicle with Steady State Constraints," AIAA Paper 2006-6558, Aug. 2006.

[16] Groves, K. P., Serrani, A., Yurkovich, S., Bolender, M. A., and Doman, D. B., "antiWindup Control for an Airbreathing Hypersonic Vehicle Model," AIAA Paper 2006-6557, Aug. 2006.

[17] Tournes, C., Landrum, D. B., Shtessel, Y., and Hawk, C. W., "Ramjet-Powered Reusable Launch Vehicle Control by Sliding Modes," *Journal of Guidance, Control, and Dynamics*, Vol. 21, No. 3, 1998, pp. 409–15.

[18] Xu, H., Mirmirani, M., and Ioannou, P., "Adaptive Sliding Mode Control Design for a Hypersonic Flight Vehicle," *Journal of Guidance, Control, and Dynamics*, Vol. 27, No. 5, 2004, pp. 829–38.

[19] Parker, J. T., Serrani, A., Yurkovich, S., Bolender, M. A., and Doman, D. B., "Control-oriented Modeling of an Airbreathing Hypersonic Vehicle," *Journal of Guidance, Control, and Dynamics*, Vol. 30, No. 3, 2007, pp. 856–869. doi:10.2514/1.27830

[20] Fiorentini, L., Serrani, A., Bolender, M., and Doman, D., "Nonlinear Robust/Adaptive Controller Design for an Airbreathing Hypersonic Vehicle Model," AIAA Paper 2007-6329, 2007.

[21] Lei, Y., Cao, C., Cliff, E., Hovakimyan, N., and Kurdila, A., "Design of an L1 Adaptive Controller for Airbreathing Hypersonic Vehicle Model in the Presence of Unmodeled Dynamics," AIAA Paper 2007-6527, Aug. 2007.

[22] Davison, E., and Goldenberg, A., "Robust Control of a General Servomechanism Problem: The Servo Compensator," *Automatica*, Vol. 11, No. 5, 1975, pp. 461–471. doi:10.1016/0005-1098(75)90022-9

[23] Davison, E., "The Robust Control of a Servomechanism Problem for Linear Time-Invariant Multivariable Systems," *IEEE Transactions on Automatic Control*, Vol. 21, No. 1, 1976, pp. 25–34. doi:10.1109/TAC.1976.1101137

[24] Stevens, B., Lewis, F., and Al-Sunni, F., "Aircraft Flight Controls Design Using Output Feedback," *Journal of Guidance, Control, and Dynamics*, Vol. 15, No. 1, 1992, pp. 238–246.

[25] Burken, J., Lu, P., Wu, Z., and Bahm, C., "Two Reconfigurable Flight-Control Design Methods: Robust Servomechanism and Control Allocation," *Journal of Guidance, Control, and Dynamics*, Vol. 24, No. 3, 2001, pp. 482–493.

[26] Isidori, A., Marconi, L., and Serrani, A., *Robust Autonomous Guidance: An Internal Model-Based Approach*, Advances in Industrial Control, Springer–Verlag, London, 2003, pp. 1–40.

[27] Davidson, J., Lallman, F., McMinn, J. D., Martin, J., Pahle, J., Stephenson, M., Selmon, J., and Bose, D., "Flight Control Laws for NASA's Hyper-X Research Vehicle," AIAA Paper 1999-4124, Aug. 1999.

[28] Schmidt, D., "Dynamics and Control of Hypersonic Aeropropulsive/Aeroelastic Vehicles," AIAA Paper 1992-4326, Aug. 1992.

[29] Schmidt, D., "Integrated Control of Hypersonic Vehicles," AIAA Paper 1993-5091, Nov. 1993.

[30] Schmidt, D., "Optimum Mission Performance and Multivariable Flight Guidance for Airbreathing Launch Vehicles," *Journal of Guidance, Control, and Dynamics*, Vol. 20, No. 6, 1997, pp. 1157–64.

[31] Schmidt, D. K., and Velapoldi, J. R., "Flight Dynamics and Feedback Guidance Issues for Hypersonic Airbreathing Vehicles," AIAA Paper 99-4122, Aug. 1999.

[32] Baruth, H., and Choe, K., "Sensor Placement in Structural Control," *Journal of Guidance, Control, and Dynamics*, Vol. 13, No. 3, 1990, pp. 524–533.

[33] Xu, K., Warnitchai, P., and Igusa, T., "Optimal Placement and Gains of Sensors and Actuators for Feedback Control," *Journal of Guidance, Control, and Dynamics*, Vol. 17, No. 5, 1994, pp. 929–934.

[34] Lim, K., "Method for Optimal Actuator and Sensor Placement for Large Flexible Structures," *Journal of Guidance, Control, and Dynamics*, Vol. 15, No. 1, 1992, pp. 49–57.

[35] Tongco, E., and Meldrum, D., "Optimal Sensor Placement of Large Flexible Space Structures," *Journal of Guidance, Control, and*

Dynamics, Vol. 19, No. 4, 1996, pp. 961–963.
[36] Bolender, M. A., and Doman, D. B., "Flight Path Angle Dynamics of Airbreathing Hypersonic Vehicles," AIAA Paper 2006-6692, 2006.
[37] Vander Velde, W., and Carignan, C., "Number and Placement of Control System Components Considering Possible Failures," *Journal of Guidance, Control, and Dynamics*, Vol. 7, No. 6, Dec. 1984, pp. 703–709.
[38] Al-Shehabi, A., and Newman, B., "Optimal Sensor Placement and Control Selection Using Mixed Gain-Phase Stabilization," AIAA Paper 2001-4032, Aug. 2001.
[39] Al-Shehabi, A., and Newman, B., "Optimal Blending Filter Parameters and Sensor Placement for Flight Control," AIAA Paper 2002-4750, Aug. 2002.
[40] Meirovitch, L., *Analytical Methods in Vibration*, McMillan, New York, 1967, pp. 135–143, 161–163.
[41] Lind, R., "Linear Parameter-Varying Modeling and Control of Structural Dynamics with Aerothermoelastic Effects," *Journal of Guidance, Control, and Dynamics*, Vol. 25, No. 4, 2002, pp. 733–739.
[42] Stevens, B. L., and Lewis, F. L., *Aircraft Control and Simulation*, 2nd ed., Wiley, New YOrk, 2003, pp. 462–470, 558–559.
[43] Rugh, W., *Linear System Theory*, 2nd ed., Prentice–Hall, Englewood Cliffs, NJ, 1996, pp. 232, 272–280.
[44] Doyle, J., and Stein, G., "Robustness with Observers," *IEEE Transactions on Automatic Control*, Vol. 24, No. 4, 1979, pp. 607–611. doi:10.1109/TAC.1979.1102095
[45] Doyle, J., and Stein, G., "*Multivariable Feedback Design: Concepts for a Classical/Modern Synthesis*," *IEEE Transactions on Automatic Control*, Vol. 26, No. 1, 1981, pp. 4–16. doi:10.1109/TAC.1981.1102555
[46] Stein, G., and Athans, M., "The LQG/LTR Procedure for Multivariable Feedback Design," *IEEE Transactions on Automatic Control*, Vol. 32, No. 2, 1987, pp. 105–114. doi:10.1109/TAC.1987.1104550
[47] Isidori, A., *Nonlinear Control Systems*, 3rd ed., Springer–Verlag, New York, 1995, pp. 137–147.
[48] Isidori, A., *Nonlinear Control Systems II*, Springer–Verlag, New York, 1999, pp. 90–98.
[49] Francis, B. A., "The Linear Multivariable Regulator Problem," *SIAM Journal on Control and Optimization*, Vol. 14, 1977, pp. 486–505.
[50] Francis, B. A., and Wonham, W. M., "The Internal Model Principle of Control Theory," *Automatica*, Vol. 12, No. 5, 1976, pp. 457–465. doi:10.1016/0005-1098(76)90006-6
[51] Kokotovic, P., O'Reilly, J., and Khalil, H., *Singular Perturbation Methods in Control: Analysis and Design*, Academic Press, Orlando, FL, 1986, pp. 47–67.
[52] Balas, M., "Feedback Control of Flexible Systems," *IEEE Transactions on Automatic Control*, Vol. 23, No. 4, 1978, pp. 673–679.